

Electronic Supplement 1

Detection capabilities of thermal sensors

Before we can apply any of the higher level analyses of Chapters 4 through 6, we need to understand the detection limits of TM-, AVHRR- and GOES-class sensors operating in the NIR, SWIR, MIR and TIR. This not only allows us to understand the size and temperature that a ground-based hot spot must achieve before it can be expected to yield useful data, but also the upper (saturation) limits of each sensor. It also allows us to understand how the data can be used for automated hot spot detection, as well as higher level analysis of sub-pixel thermal structure and heat flux. In this supplement we thus first explore the detection limits of TM-, AVHRR- and GOES-class sensors, before examining the likely thermal surface that a pixel over a volcanic hot spot will contain, sensor response over a thermally mixed pixel and pixel-integrated temperature.

S1.1 Satellite sensor detection capabilities

Work exploring the detection satellite-based sensor capabilities, limits and response over hot targets represents the ground-work necessary if the methodologies and applications reviewed in Chapters 4 through 6 are to be developed and applied. As a result, from the mid-1990s onwards, a number of papers began to include detection issues as part of a wider consideration of the application of satellite-sensor-derived thermal data to volcanological problems, with Appendix A identifying 34 papers published between 1965 and 2005 dealing, in whole or in part, with detection issues at lava lakes, channels, flows, domes and fumarole fields. Understanding the detection capabilities of satellite-based sensors operating in the infrared is thus the first of the five major theme areas identified in Chapter 1. We begin with a brief review of work dealing with detection capabilities of satellite-based thermal sensors as collated in Appendix A.

During the early-to-mid 1990s, a series of papers were published dealing with the detection capabilities of satellite sensors over active volcanic hot spots. Initially two papers, those of Oppenheimer and Rothery (1991) and Oppenheimer *et al.* (1993a), considered the ability of sensors operating in the SWIR and TIR to detect and measure the radiant heat flux at open vents, fumarole fields and lava lakes. Next, two papers by Flynn and Mouginiis-Mark (1992; 1994) considered the potential response of AVHRR's NIR band (band 2) over active lava channels. A third paper by Flynn and Mouginiis-Mark (1995)

considered the thermal characteristics of active lava flows and fires using SWIR and TIR data from Landsat TM.

The exploration of AVHRR-class data for hot spot detection really took off with a series of papers beginning in 1994 which explored viewing geometry issues in AVHRR-class data, as well as the detection capabilities of AVHRR itself over volcanic hot spots. The effects of viewing geometry on hot spot detection and measurement in AVHRR and ATSR data, for example, were addressed in a series of papers by Mouginiis-Mark *et al.* (1994), Harris *et al.* (1997a; 1999), and Wooster *et al.* (1998). These studies included consideration of variation in pixel-integrated temperature due to (i) changing pixel size with scan angle (Mouginiis-Mark *et al.* 1994; Harris *et al.*, 1997a), (ii) pixel response function (Wooster *et al.*, 1998), and (iii) topographic shielding (Harris *et al.*, 1997a, 1999; Wooster *et al.*, 1998). At the same time, the detection capabilities of AVHRR data collected over active lava flows were assessed in a parallel series of papers which considered:

- (i) the response of AVHRR's NIR, MIR and TIR bands to particularly intense volcanic heat sources using Krafla's 1984 fissure eruption as a case study (Harris *et al.*, 1995a),
- (ii) the upper detection (saturation) limits of the AVHRR sensor (Harris *et al.*, 1995b), and
- (iii) detection of lava flows and lakes of various sizes, as well as hot vents and fumaroles, in AVHRR data (Harris *et al.*, 1997a; Harris and Stevenson, 1997).

These efforts culminated in the recovery of sub-pixel thermal structures from satellite-based data, as well as their conversion to heat flux and discharge rate, as considered in Chapter 4. They also provided the ground work necessary for the development of a series of automated hot spot detection algorithms, considered in Chapter 5, as well as a number of time-series-based studies, as reviewed in Chapter 6.

SI.1.1 Detection: lower limits

To be detected, the volcanic hot spot must be of sufficient temperature so as to register the minimum radiance that a sensor can detect. That is, the surface emitted radiance must be sufficient to register a digital number (DN) at the satellite-based sensor of one (see Chapter 3 for definition of DN). The at-sensor radiance (R_{\min}^*) necessary to achieve the DN of one¹ (DN_{\min}) can be calculated using the sensor calibration coefficients as follows:

$$R_{\min}^* = a DN_{\min} + b \quad (S1.1)$$

where a and b are the calibration coefficients for the sensor and band of interest (see Electronic Supplement 2). Parameter R_{\min}^* defines the smallest amount of emitted radiance that can be detected by the sensor. By way of example, values of R_{\min}^* for the NIR, SWIR, MIR and TIR bands of TM, AVHRR and GOES are calculated using typical calibration coefficients for each sensor in Electronic Supplement 2.

¹ If the calibration is inverse, then instead this will be a DN of 255 or 1024 (see Appendix H)

Table S1.1. *Minimum and maximum recordable radiances, and temperatures that these yield, for TM, AVHRR and GOES. Values are calculated using the calibration procedures with the minimum and maximum DN and calibration coefficients for each sensor given in Electronic Supplement 2. Values for TM are obtained using the coefficients of Chander and Markham (2003) (see Table S2.1). Values for AVHRR are for NOAA-12 and include non-linear correction (see AVHRR section of Electronic Supplement 2), and those for GOES are for the Imager aboard GOES-12 (see Table S2.8).*

Sensor	Band	Spectral Region	R_{\min}^* ($W\ m^{-2}\ m^{-1}$)	R_{\max}^*	T_{\min} ($^{\circ}C$)	T_{\max} ($^{\circ}C$)
TM	3	NIR	2.86E+06	8.29E+08	777	1171
TM	4	SWIR	2.01E+06	6.94E+08	595	954
TM	5	SWIR	3.44E+05	9.49E+07	203	415
TM	7	SWIR	1.44E+05	5.18E+07	94	277
GOES	2	MIR	1.57E+04	8.60E+06	-57	69
AVHRR	3	MIR	1.15E+04	3.60E+06	-57	49
GOES	4	TIR	2.23E+05	5.27E+07	-130	68
TM	6	TIR	4.06E+06	4.81E+07	-69	66
AVHRR	4	TIR	1.75E+05	4.62E+07	-134	58

Using the Planck function (see Chapter 2), we can convert our R_{\min}^* values to temperature equivalents, thereby defining the temperature a surface has to achieve before it can be detected in a certain band, as done in Table S1.1. To be truly detectable, the signal must exceed the sensor $NE\Delta T$, i.e., the variation in temperature due to noise (see Chapter 3). However, $NE\Delta T$ values (as given in Appendices D to F) are typically less than 0.5 K.

From Table S1.1 we see that, as we move from the TIR to the NIR, so the minimum detectable temperature increases. This is due to one of the first basic physical principles covered in Chapter 2: because spectral radiant exitance from blackbodies at earth ambient temperatures becomes extremely small in the SWIR, ambient sources emit insufficient radiance to be detected at these wavebands. Thus, as the wavelength becomes smaller, so the temperature the source must attain has to be higher before it can attain an emission level that can be detected. Thus, the NIR band (band 3) of TM requires a pixel-filling source of $\sim 780\ ^{\circ}C$ before it can be detected. As we move to the SWIR wavelengths, the detection limit decreases to $595\ ^{\circ}C$ for TM band 4 and to $94\ ^{\circ}C$ for band 7. Once we reach the TIR (band 6) the detection limit is $-69\ ^{\circ}C$.

S1.1.2 Detection: upper limits (saturation)

The sensor will also have an upper limit, beyond which point radiance from the source may increase, but no higher value will be registered. This is the saturation point of the sensor (R_{\max}^*). This will occur at the maximum DN that can be

registered. Saturation point can thus be calculated using the radiance necessary to achieve a DN of 255 (D_{\max})² in:

$$R_{\max}^* = a DN_{\max} + b \quad (\text{S1.2})$$

Parameter R_{\max}^* thus defines the greatest amount of emitted radiance that can be detected by the sensor. By way of example, values of R_{\max}^* for the NIR, SWIR, MIR and TIR bands of TM, AVHRR and GOES are calculated using typical calibration coefficients for each sensor in Electronic Supplement 2.

As with R_{\min}^* , we can convert our R_{\max}^* values to temperatures, thereby defining the temperature a surface has to achieve to saturate in a certain band, as done in Table S1.1. Once saturation temperature is reached, we do not know exactly what temperature the surface is at, all that we know is that the surface is at a temperature that is greater than or equal to the saturation temperature. From Table S1.1, we see that as we move from the NIR to the TIR, so the saturation temperature decreases. A review of the saturation temperatures given for TM-, AVHRR- and GOES-class sensors, as given in Table S1.2, shows that saturation for most TIR sensors is reached at between 50 and 90 °C. For SWIR and NIR sensors, saturation levels are higher, being up to 470 °C in the SWIR and 1000 °C to 1200 °C in the NIR.

S1.1.3 Sensor dynamic range, band width and the Planck function

The minimum and maximum detection limits defined by R_{\min}^* and R_{\max}^* delimit the sensor dynamic range. Any radiances between the two limits can be detected and measured by the sensor. Hence, the radiance ranges defined by the R_{\min}^* and R_{\max}^* detection limits in Table S1.1 give the nominal dynamic ranges for TM, AVHRR and GOES.

Radiances falling below the lower limit of the sensor dynamic range will not be detected; those falling above it will saturate the sensor and be represented by the maximum recordable value. A wide dynamic range allows a wide range of temperatures to be measured, but at the expense of precision. For example, from Table S1.1 we see that for Landsat Tm band 7 a DN of zero relates to a temperature of 94 °C and a DN of 255 to 277 °C; the sensor dynamic range thus spans 183 °C with increments of 0.72 °C over the 0–255 DN dynamic range. In contrast, for band 6 the dynamic range extends from –69 °C to 66 °C and thus spans 135 °C with increments of 0.53 °C. It is also important to understand where the upper and lower limits of the sensor dynamic range lie to determine whether a certain thermal feature can be detected or not.

Plotting the sensor dynamic range over Planck curves is thus instructive for three reasons. First, it plots the location of the waveband in relation to the point of peak emission for a body of given temperature. Second, it reveals the temperature a body must reach to first be detected and then to saturate a sensor waveband. Third, we can assess how steeply a Planck curve ascends, or descends, across a given bandwidth and dynamic range combination. In Figure S1.1 we plot the dynamic ranges and bandwidths for the NIR, SWIR, MIR

² If the calibration extends to 1024, then this will be 1024. Alternatively, if the calibration is inverse, then this will be a DN of 0.

Table S1.2. Saturation temperatures and temperature of peak emission for main TM-, AVHRR-, and GOES-class sensors. Table is sequenced in order of increasing wavelength, showing that as wavelength increases from the NIR through the SWIR MIR to TIR, so saturation temperature decreases. Nominal saturation temperatures are given here and are taken from the generic sensor parameter Tables given in Appendices C, D, and E. Note that actual saturation temperatures may diverge by a few degrees centigrade from the nominal values given here depending on variations in calibration with time and between instruments. For example, saturation temperature for band 4 of the AVHRR aboard NOAA-9 was $\sim 55^\circ\text{C}$, but for that aboard NOAA-11 it was $\sim 70^\circ\text{C}$. The nominal value is 60°C .

Sensor	Band	Spectral Region	Waveband (μm)	Saturation Temperature ($^\circ\text{C}$)	Temperature of peak emission ($^\circ\text{C}$)
TM	3	NIR	0.63 – 0.69	1170	4118
TM	4	NIR	0.76 – 0.90	950	3219
TM	5	SWIR	1.55 – 1.75	415	1483
ATSR		SWIR	1.6	260	1538
ASTER	4	SWIR	1.600 – 1.700	466	1483
MODIS	6	SWIR	1.628–1.652	470	1494
TM	7	SWIR	2.08 – 2.35	280	1035
MODIS	7	SWIR	2.105–2.155	300	1088
ASTER	5	SWIR	2.145 – 2.185	385	1066
ASTER	6	SWIR	2.185 – 2.225	376	1041
ASTER	7	SWIR	2.235 – 2.285	358	1009
ASTER	8	SWIR	2.295 – 2.365	330	971
ASTER	9	SWIR	2.360 – 2.430	326	937
AVHRR	3	MIR	3.55 – 3.93	50	502
ATSR		MIR	3.7	50	510
GOES	2	MIR	3.80 – 4.00	62	470
MODIS	21	MIR	3.929–3.989	180	459
MODIS	22	MIR	3.929–3.989	60	459
ASTER	10	TIR	8.125 – 8.475	90	76
ASTER	11	TIR	8.475 – 8.825	90	62
ASTER	12	TIR	8.925 – 9.275	90	45
GOES	4	TIR	10.2 – 11.2	47	-2
ASTER	13	TIR	10.25 – 10.95	90	0
AVHRR	4	TIR	10.3 – 11.3	60	-5
TM	6	TIR	10.4 – 12.5	70	-20
ATSR		TIR	10.8	50	-5
ASTER	14	TIR	10.95 – 11.65	90	-17
AVHRR	5	TIR	11.5 – 12.5	60	-32
GOES	5	TIR	11.5 – 12.5	47	-32
MODIS	32	TIR	11.770– 12.270	130	-32
ATSR		TIR	12.0	50	-32

and TIR wavebands of TM, AVHRR and GOES. Wein's displacement law can also be rearranged to estimate the temperature of peak emission (T_m) for a given wavelength (λ) through:

$$T_m = \frac{2898 \mu m K}{\lambda} \quad (K) \quad S1.3$$

These values are given for the mid-point of each sensor wavelength range in Table S1.2.

Dynamic ranges in the NIR and SWIR

From Figure S1.1 we notice that, as we move to shorter wavelengths across the SWIR and NIR, so the location of the sensor dynamic range moves up the x-axis. That is, the minimum radiance that can be detected increases, as does the saturation radiance. In terms of temperature this means that, as we move to shorter wavelengths, so the temperature a body must attain has to increase before it is detectable. The corollary is that higher maximum temperatures can be recorded as we move towards the NIR. This is apparent from Table S1.1 where, for example, we see that the dynamic range of TM's SWIR band 7 spans 94 °C to 277 °C. In

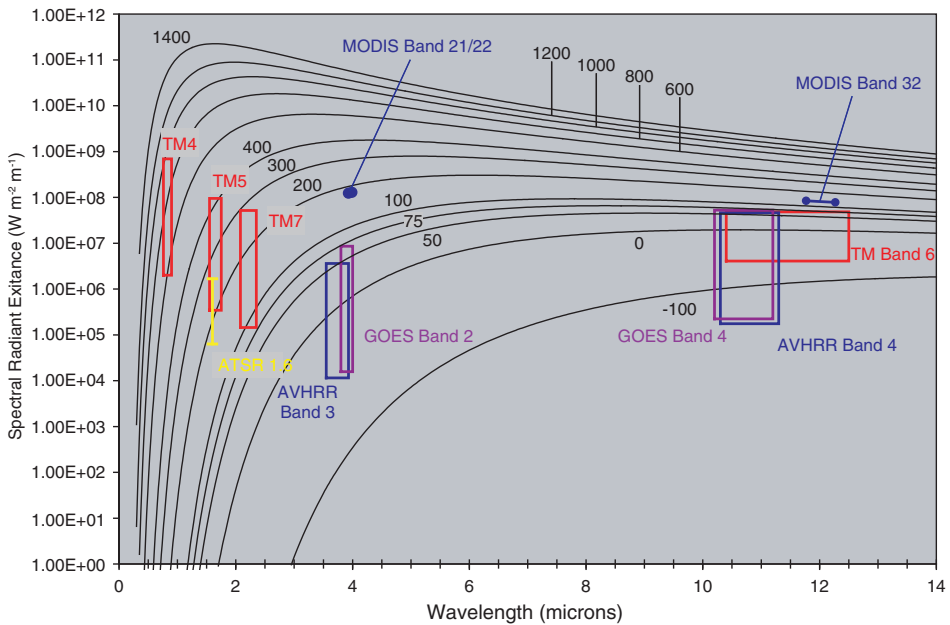


Figure S1.1 Planck curves for blackbody spectral emission from surfaces at temperatures between minus 100 °C and 1400 °C, with the waveband and dynamic range for some selected sensors. In each case, the height of the box defined for each sensor defines the dynamic range, and width defines sensor wavelength range. The plot can be used to assess detection and saturation limits: Planck curves passing below a box will define temperatures that are not detectable by the sensor; those passing above a box will exceed the upper limit of the sensor's dynamic range, thus causing saturation; those passing through the box will register measurable, unsaturated spectral radiance.

contrast, TM's NIR band 3 does not begin to detect until around 780 °C, but is capable of measuring temperatures up to 1170 °C. Thus, sensors operating in the SWIR and NIR have dynamic ranges suitable for measuring high-temperature bodies.

Dynamic ranges in the MIR and TIR

As can be seen from Figure S1.1, sensors operating in the MIR and TIR tend to span similar dynamic ranges. Table S1.1 shows that this typically spans -70 °C to $+70$ °C. Given that all TM-, AVHRR- and GOES-class sensors have MIR and TIR bands with dynamic ranges that extend well below the 0 °C radiance equivalent, it is the upper limit (i.e., the maximum temperature that can be measured) that becomes crucial at these wavelengths. Table S1.2 gives the dynamic range upper limits, or saturation temperatures, for the primary TM-, AVHRR- and GOES-class sensors. We see that most sensors in the MIR and TIR have dynamic ranges that extend to 50 °C or 70 °C. The exception is the TIR bands of ASTER which extend to 90 °C, and MODIS MIR band 21 which has an upper limit of 180 °C. Thus, unlike sensors operating in the SWIR, sensors in the MIR and TIR have dynamic ranges which cover ambient Earth temperatures, with ranges which extend downwards to cover low temperature sources such as high cloud and ice.

The MIR and TIR band widths differ in respect to their position in relation to the point of peak emission. In Table S1.2 we see that sensors in the MIR coincide with peak emission from bodies at between 460 °C and 510 °C; those in the TIR coincide with peak emission from bodies at 60 °C (8.7 μm), 0 °C (10.6 μm) and -30 °C (11.9 μm). Thus, only sensors in the TIR coincide with the wavelength of peak emission for sources at Earth ambient temperatures; those in the SWIR and MIR coincide with peak emission from high temperature sources. Table S1.2 shows that peak emission in the SWIR is experienced by bodies at between 940 °C and 1480 °C. For wavebands in the NIR, this increases to between 3000 °C and 4000 °C.

Slope of the Planck curve across the sensor bandwidth and sensor-recorded temperature

From Figure S1.1 we see that the Planck curves for sources at 0 °C to 600 °C ascend quite steeply across the NIR and SWIR band widths, but are relatively flat across the TIR band widths. As discussed in Chapter 3, the slope of the Planck curve within a sensor band width will affect the difference between the actual source temperature and the temperature recorded by the sensor. In cases where the radiance is distributed quite evenly across the bandwidth, the difference between the source temperature and the temperature recorded by the sensor will be small. However, where the radiance is distributed unevenly across the bandwidth, then the difference will be large. This will dictate whether temperature retrieval will require convolution of the Planck function with the sensor response function, as done in Appendix C.

The effect of uneven radiance distribution across a given bandwidth on sensor-recorded temperature can be assessed by modifying Equation (3.15b) of Chapter 3. That is, the at-sensor radiance (R_{sensor}) from a source at temperature, T , can be obtained from:

$$R_{\text{sensor}} = \frac{\int_{\lambda_{\min}}^{\lambda_{\max}} M(\lambda, T) d\lambda}{\int_{\lambda_{\min}}^{\lambda_{\max}} d\lambda} \quad (\text{W m}^{-2} \text{ m}^{-1}) \quad (\text{S1.4})$$

Where λ_{\max} and λ_{\min} are the upper and lower sensor waveband limits. In other words, the waveband is split into n increments of width $d\lambda$ and the spectral radiance is calculated for each increment. These values are then summed and divided by the sensor band width. Converting the resulting radiance (R_{sensor}) to a temperature will give the sensor-recorded temperature (T_{sensor}) for a source at temperature T emitting within the given bandwidth, where the bandwidth is defined by λ_{\max} minus λ_{\min} .

We solve Equation (S1.4) for a range of source temperatures and sensor bandwidths in Table S1.3. The difference between the source temperature (given along the top row of Table S1.3) and the sensor recorded temperature (given within the body of Table S1.3) shows the effect of varying emission across each sensor bandwidth on recorded temperature. For most bands operating at wavelengths greater than 1.5 μm , the difference between the source and sensor recorded temperature is less than 3 $^{\circ}\text{C}$, and typically less than 2 $^{\circ}\text{C}$. For all TIR and MIR bands the difference is often close to zero. However, the magnitude of the difference varies depending on wavelength, source temperature and bandwidth. Thus, from Table S1.3, we see the following:

- As we move to longer wavelengths so the difference between the source and sensor-recorded temperature decreases. We can see this by looking down each column of Table S1.3. If we consider a source temperature of 250 $^{\circ}\text{C}$, for example, the sensor recorded temperature in TM's NIR band (band 3) will be 256 $^{\circ}\text{C}$. However, for most bands in the TIR, the sensor recorded temperature is within a degree of the source temperature. This is a result of the Planck curves having relatively steep slopes across NIR bandwidths. In contrast, across TIR bandwidths they are relatively flat, as can be seen in Figure S1.1. Thus the distribution of radiance is much more evenly distributed across the TIR bandwidths.
- As source temperature increases so the difference between the source and sensor-recorded temperature changes. We can see this by looking across each row of Table S1.3. For example, for TM's SWIR band 5 as we move from a source temperature of 100 $^{\circ}\text{C}$ to one of 1000 $^{\circ}\text{C}$ the difference decreases from 12 $^{\circ}\text{C}$ to 7 $^{\circ}\text{C}$. The reason for this change is apparent from Figure S1.1. Planck curves ascend steeply across this waveband, but as source temperature increases between 100 $^{\circ}\text{C}$ and 1000 $^{\circ}\text{C}$ so the slope of the curve decreases. As a result, the radiance becomes more evenly distributed across the band width as the source temperature increases. In the TIR, the situation is reversed. For example, for TM band 6 as we move from a source temperature of 100 $^{\circ}\text{C}$ to 1000 $^{\circ}\text{C}$ the difference between the source and sensor recorded temperatures increases from 0.3 $^{\circ}\text{C}$ to 10 $^{\circ}\text{C}$. The reason for this is again apparent from Figure S1.1. In this spectral region the Planck curves are descending through the sensor bandwidth, with the slope of

the descent increasing with increased temperature. As a result, the radiance becomes more evenly distributed across the band pass as source temperature decreases. Radiance is most evenly distributed across a given bandwidth in situations where the waveband coincides with the point of peak emission. Thus, for sensors operating on the MIR at 3.5 to 4.0 μm , the difference between the source and sensor recorded temperature is essentially zero for source temperatures of 450 $^{\circ}\text{C}$ to 500 $^{\circ}\text{C}$. Table S1.2 shows that this is the temperature of peak emission for these wavebands, with Figure S1.1 showing that the Planck curves for sources at such temperatures are more-or-less flat across the MIR bandwidths.

- As the bandwidth increases so too does the difference between the source and sensor-recorded temperatures, as bands with greater widths experience greater variation in radiance across the bandwidth. This effect is most apparent in the panchromatic band of ETM+ (band 8: 0.52 to 0.9 μm), a band which spans the VIS (red), NIR and SWIR portions of the spectrum. As shown in Figure 3.16 of Chapter 3, for sources at 600 $^{\circ}\text{C}$ to 1100 $^{\circ}\text{C}$ radiance varies greatly across this broad bandwidth, increasing from near zero at the VIS end of the band. As a result, for the source temperatures considered in Table S1.3, the difference between the source and sensor-recorded temperatures ranges from 56 $^{\circ}\text{C}$ to 79 $^{\circ}\text{C}$. For narrower bands within this bandwidth the difference is less extreme. For example, for TM's NIR band (band 3: 0.63 to 0.69 μm) differences are less than 6 $^{\circ}\text{C}$. We see the same effect in the MIR and TIR, although the effect is less extreme at these longer wavelengths. For example, MODIS band 21 and AVHRR band 3 both operate in the MIR, however the bandwidths are 0.06 μm and 0.38 μm , respectively. For MODIS band 21 the differences between the source and sensor-recorded temperatures given in Table S1.3 are close to zero. For the broader MIR band of AVHRR we see greater differences, although the difference is small, being no greater than 1 $^{\circ}\text{C}$. The effect is more extreme for TM's TIR band (band 6) due to its rather broad bandwidth of 2.1 μm . For source temperatures considered in Table S1.3, the difference between the source and sensor-recorded temperatures for TM band 6 can be as great as 10 $^{\circ}\text{C}$ for a source temperature of 1000 $^{\circ}\text{C}$. The difference is typically less than 1 $^{\circ}\text{C}$ (being 0.3 $^{\circ}\text{C}$ to 0.5 $^{\circ}\text{C}$) for source temperatures less than 250 $^{\circ}\text{C}$. However, these differences compare with differences of less than two tenths of a degree centigrade (for sources at ≤ 250 $^{\circ}\text{C}$) for all other TIR bands considered in Table S1.3 which have much narrower (≤ 1 μm) bandwidths.

Slope of the Planck curve across the sensor waveband and temperature retrieval

In effect the analysis completed as part of Table S1.3 provides an error assessment for temperature retrieval using waveband mid-points as opposed to convolution of the Planck function across the sensor bandwidth, as done in Appendix C. We see that, for most cases, waveband mid-points can be used to retrieve temperature to within one degree Centigrade. Table S1.3 shows that the exceptions are:

Table S1.3. *Difference between source and sensor recorded temperatures for sensors operating in the NIR, SWIR, MIR and TIR.*

Sensor-Band	Spectral Region	Waveband (μm)	Band Width (μm)	Source Temperature ($^{\circ}\text{C}$)					
				50	100	250	500	750	1000
ETM+-8	VIS-NIR-SWIR	0.52–0.9	0.38	106	161	322	579	826	1068
TM-3	NIR	0.63–0.69	0.06	55	105	256	505	755	1004
TM-4	SWIR	0.76–0.9	0.14	62	112	262	511	759	1007
TM-5	SWIR	1.55–1.75	0.20	53	103	253	502	751	1000
TM-7	SWIR	2.08–2.35	0.27	52	102	251	500	750	999
AVHRR-3	MIR	3.55–3.93	0.38	51	100	250	500	749	999
MODIS-21	MIR	3.929–3.989	0.06	50	100	250	500	750	1000
ASTER-10	TIR	8.125–8.475	0.35	50.0	100.0	249.9	499.7	749.6	999.4
ASTER-12	TIR	8.925–9.275	0.35	50.0	100.0	249.9	499.7	749.6	999.4
AVHRR-4	TIR	10.3–11.3	1.0	49.9	99.8	249.8	500.0	750.4	1000.8
AVHRR-5	TIR	11.5–12.5	1.0	49.9	99.9	249.9	500.0	750.2	1000.5
MODIS-32	TIR	11.77–12.27	0.5	49.9	99.9	249.8	499.7	749.5	999.4
TM-6	TIR	10.4–12.5	2.1	49.6	99.7	250.5	503.0	756.3	1010.0

- All wavebands operating at less than 1 μm ,
- Wavebands at 1.55 to 1.75 μm for temperatures less than 500 $^{\circ}\text{C}$,
- Wavebands at 2.08 to 2.35 μm for temperatures less than 250 $^{\circ}\text{C}$,
- Broad bandwidths in the TIR for temperatures greater than 500 $^{\circ}\text{C}$.

These cases have to be assessed in terms of the sensor dynamic range. For example, the second and third cases relate to TM bands 5 and 7. From Table S1.1 we see that while the dynamic range of TM band 5 is 203 $^{\circ}\text{C}$ to 415 $^{\circ}\text{C}$, that of band 7 is 94 $^{\circ}\text{C}$ to 277 $^{\circ}\text{C}$. Thus, we will be dealing with temperatures less than 500 $^{\circ}\text{C}$ in TM band 5, and less than 250 $^{\circ}\text{C}$ in band 5. As a result error will be greater than 1 $^{\circ}\text{C}$ in both bands. Reference to Table S1.3 shows that we may expect an overestimate of source temperature by ~ 3 $^{\circ}\text{C}$ across the dynamic range of TM band 5 if we use the waveband midpoint to convert radiance to brightness temperature. For band 7, the error will be between 1 $^{\circ}\text{C}$ and 2 $^{\circ}\text{C}$. The final case in the above listing relates to TM band 6. This band has a dynamic range of -69 $^{\circ}\text{C}$ to $+66$ $^{\circ}\text{C}$. We are thus not dealing with temperatures greater than 500 $^{\circ}\text{C}$, so error will be less than 1 $^{\circ}\text{C}$. Reference to Table S1.3 shows that we may expect an overestimate of source temperature by less than 0.5 $^{\circ}\text{C}$ across the dynamic range of TM band 6 if we use the waveband midpoint to convert radiance to brightness temperature. Only if the band 6 dynamic range extended to higher temperatures would we encounter error of greater than 1 $^{\circ}\text{C}$.

For the dynamic ranges of all TIR and MIR bands considered in Table S1.3 (typically $-70\text{ }^{\circ}\text{C}$ to $+70\text{ }^{\circ}\text{C}$) the difference between the temperature retrieved using waveband mid-points and that obtained from convolution of the Planck function across the sensor band width will be close to zero. However, differences of a few 10^{th} s of a degree do still exist in the MIR and TIR. Thus, for example, in the GOES calibration routine a small correction is applied to GOES-derived brightness temperature to take such effects into account, as shown in Electronic Supplement 2. Such corrections are thus required if a precision of less than $0.1\text{ }^{\circ}\text{C}$ is required in the MIR and TIR. Correction is also required if a precision of less than $1\text{ }^{\circ}\text{C}$ to $3\text{ }^{\circ}\text{C}$ (the error varying depending on waveband location, dynamic range and bandwidth) is required in the SWIR.

S1.2 Thermal structures and pixel-integrated temperature

Whether a surface can be detected by a sensor depends on its temperature. That is, the temperature of the surface must be sufficient so as to emit a radiance that falls within the dynamic range of the sensor. If the surface is too cool, then the radiance emitted will be less than the lower end of the dynamic range, and the body will not be detected. Conversely, if the surface becomes sufficiently hot, then the radiance emitted will exceed the sensor dynamic range so that the measurement will be saturated. Thus, to assess the detection capabilities of sensors operating in the NIR, SWIR, MIR and TIR we must also assess the likely surface temperatures and thermal structures encountered over active volcanic phenomena. We also need to define ‘‘pixel-integrated temperature’’.

S1.2.1 Two- and three-component thermal models for pixels over active lavas

It is unlikely that the surface of an active lava flow will be described by a single temperature. Instead, temperature may vary by hundreds of degrees over spatial scales of less than a meter, even less than a centimeter. Thus, the classic model of Crisp and Baloga (1990) describes the thermal structure for the surface of an active lava flow in terms of two thermal components. This model is given graphically in Figure 4.6b of Chapter 4 where a relatively cool, chilled crust forming on the flow surface is broken by high temperature cracks at which the upper levels of the hot interior are exposed. A pixel containing such a surface will thus contain two thermal components, the high temperature cracks at temperature T_h occupying portion p of the pixel, surrounded by cooler crust at temperature T_c which occupies the remainder (i.e., $1 - p$) of the pixel. The spectral radiant exitance for such a pixel will be described by:

$$M(\lambda, T_{\text{int}}) = p M(\lambda, T_h) + (1 - p)M(\lambda, T_c) \quad (\text{S1.5a})$$

in which T_{int} is the pixel-integrated temperature. For a pixel of area A_{pixel} , the portion occupied by the hot cracks can be estimated from the crack area (A_{crack}) as follows:

$$p = \frac{A_{\text{crack}}}{A_{\text{pixel}}} \quad (\text{S1.5b})$$

where A_{crack} must be less than or equal to A_{pixel} so that p is less than or equal to one. Thus Equation (S1.5a) can also be written in terms of the area of the two thermal components:

$$M(\lambda, T_{\text{int}}) = \frac{A_{\text{crack}}}{A_{\text{pixel}}} M(\lambda, T_{\text{h}}) + \left(1 - \frac{A_{\text{crack}}}{A_{\text{pixel}}}\right) M(\lambda, T_{\text{c}}) \quad (\text{S1.5c})$$

The model for pixel-integrated temperature given in Equation (S1.5a) applies to an active lava body that is sufficiently large to fill a pixel. As the body becomes smaller, or the pixel becomes larger, a third thermal component has to be considered, that is ambient ground at temperature T_{a} which surrounds the active lava. The spectral radiant exitance for such a pixel will thus be described by a three component model, whereby:

$$M(\lambda, T_{\text{int}}) = p M(\lambda, T_{\text{h}}) + p_{\text{c}} M(\lambda, T_{\text{c}}) + (1 - p - p_{\text{c}}) M(\lambda, T_{\text{a}}) \quad (\text{S1.6a})$$

What this Equation says is that the high temperature cracks occupy portion p of the pixel, the chilled crust occupies portion p_{c} , and the ambient ground occupies the remainder (i.e., $1 - p - p_{\text{c}}$) of the pixel. In this case, the pixel portion occupied by the hot cracks can be estimated from the crack area (A_{crack}) using Equation (S1.5) and the portion occupied by the crust from the crust area (A_{crust}) using:

$$p_{\text{c}} = \frac{A_{\text{crust}}}{A_{\text{pixel}}} \quad (\text{S1.6b})$$

We note now that the sum of A_{crack} and A_{crust} must be less than or equal to A_{pixel} so that $p + p_{\text{c}}$ is less than or equal to one [i.e., $p + p_{\text{c}} + (1 - p - p_{\text{c}})$ must sum to one and all values must be positive]. Thus, as with Equation (S1.5a), Equation (S1.6a) can also be written in terms of the area of the two active lava thermal components:

$$M(\lambda, T_{\text{int}}) = \frac{A_{\text{crack}}}{A_{\text{pixel}}} M(\lambda, T_{\text{h}}) + \frac{A_{\text{crust}}}{A_{\text{pixel}}} M(\lambda, T_{\text{c}}) + \left(1 - \frac{A_{\text{crack}} + A_{\text{crust}}}{A_{\text{pixel}}}\right) M(\lambda, T_{\text{a}}) \quad (\text{S1.6c})$$

S1.2.2 Pixel-integrated temperature

Equations (S1.5) and (S1.6) introduce the concept of pixel-integrated temperature (T_{int}). Where a pixel is occupied by more than one thermal component, the pixel brightness temperature will be the result of integrating the radiance emitted by a number of thermal sources within the pixel. Thus, for the case given in Equation (S1.5), the pixel-integrated temperature is not that of the chilled crust, nor that of the high temperature cracks, but some weighted value that will fall between the two end member temperatures.

The weighting of the value depends on the relative size of the two thermal components, as well as wavelength. This is shown in Figure S1.2 where we consider the pixel-integrated temperature in the NIR, SWIR, MIR and TIR for a lava surface composed of hot cracks at 1000 °C surrounded by a chilled crust at 200 °C. The portion occupied by the hot cracks is varied between zero and one. As we move along the x-axis of Figure S1.2 we see the effect

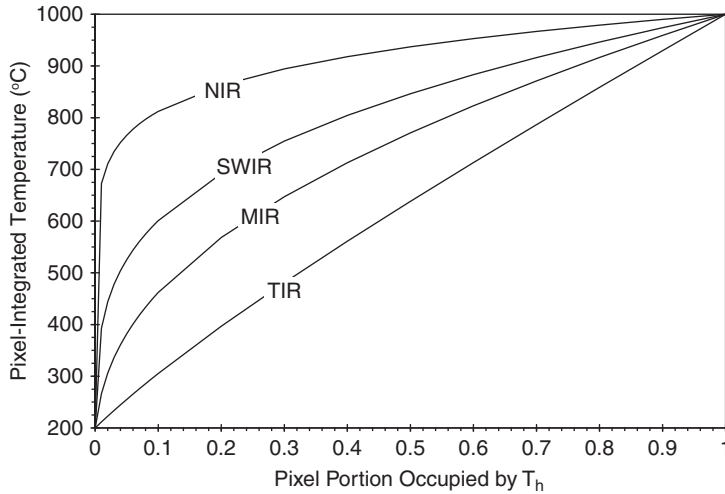


Figure S1.2 Increase in pixel-integrated temperature with portion of pixel occupied by a hot spot at T_h in the NIR, SWIR, MIR and TIR. For this model a hot spot at 1000 °C is set against a background at 200 °C, so that when $p = 0$ (i.e., the pixel is filled by the background source at 200 °C) the pixel-integrated temperature is 200 °C, and when $p = 1$ (i.e., the pixel is filled by the hot source at 1000 °C) the pixel-integrated temperature is 1000 °C.

of increasing the size of the hot crack component: the pixel-integrated temperature increases from 200 °C, the crust temperature at $p = 0$ (i.e., the pixel is filled with the crust component), to 1000 °C, the crack temperature at $p = 1$ (i.e., the pixel is filled with the crack component).

If we compare the variation in pixel-integrated temperature with increased p in the NIR, SWIR, TIR and MIR, we see that whether the pixel-integrated temperature is weighted towards the crack or the crust temperature depends on wavelength. Take, for example, a situation where the pixel is 10 % filled with high temperature crack ($p = 0.1$). For the TIR, the pixel-integrated temperature is weighted towards the crust temperature, it being 305 °C. In contrast, for the NIR it is weighted towards the crack temperature, it being 812 °C. The reason for this can be understood by examining the Planck curves for these two temperatures. If we examine Figure S1.1 we see that Planck curves for bodies at 200 °C and 1000 °C are widely separated in the NIR. As a result, levels of radiance emitted by bodies at the two temperatures are very different, the radiance equivalents for the two temperatures being $1.41 \times 10^9 \text{ W m}^{-2} \text{ m}^{-1}$ and $2.42 \times 10^{-1} \text{ W m}^{-2} \text{ m}^{-1}$ at $0.85 \mu\text{m}$. In contrast, Planck curves for bodies at 200 °C and 1000 °C are not so widely separated in the TIR. As a result, levels of radiance emitted by bodies at the two temperatures are not so different, the radiance equivalents for the two temperatures being $1.29 \times 10^9 \text{ W m}^{-2} \text{ m}^{-1}$ and $1.56 \times 10^8 \text{ W m}^{-2} \text{ m}^{-1}$ at $11 \mu\text{m}$. Thus, the relative contribution of the high temperature crack component to the pixel-integrated radiance is much greater in the NIR than in the TIR. As a result, the pixel-integrated temperature becomes increasingly weighted towards the temperature of the crack component as we move from the TIR to the NIR, as is apparent from Figure S1.2.

S1.3 Detection

We will now use the above pixel mixture models, along with field data for high temperature volcanic phenomena, to consider the upper and lower detection limits of TM-, AVHRR- and GOES-class detectors operating between the NIR and TIR.

S1.3.1 Thermal structures and detection of active lava lakes

The size and temperature of the thermal components that comprise the surface of an active lava lake were estimated by Flynn *et al.* (1993) using spectroradiometer data obtained for the active lava lake of Kupaianaha, Kilauea (Hawaii) during 1987 and 1988. The results of the two-component model applied by Flynn *et al.* (1993) to their data are given in Table S1.4 along with the pixel-integrated temperatures that these yield in the NIR, SWIR, MIR and TIR if the lake surface fills the pixel.

Table S1.4. Lava lake hot crack temperature and area, as well as crust temperature, from Table 1 of Flynn *et al.* (1993). Portion of the surface occupied by the crack component is calculated from A_h using Equation (S1.5b) and an A_{pixel} of 0.23 m^2 as given by Flynn *et al.* (1993). Temperature data were converted to radiances in the NIR ($\lambda = 0.85 \mu\text{m}$), SWIR ($\lambda = 2.25 \mu\text{m}$), MIR ($\lambda = 3.75 \mu\text{m}$) and TIR ($\lambda = 11 \mu\text{m}$) using the Planck Function [Equation (2.4) of Chapter 2]. Pixel-integrated radiances in the NIR, SWIR, MIR and TIR can then be calculated using Equation (S1.5a). Finally, pixel-integrated radiance is converted to temperature by using the inversion of the Planck Function as given in Equation (2.5) of Chapter 2.

Case	T_h (°C)	T_c (°C)	A_h (m ²)	p	Pixel-Integrated Temperature (°C)			
					NIR	SWIR	MIR	TIR
Type 1								
1	900	400	9.10E-03	3.96E-02	686	495	444	422
2	1100	572	3.10E-03	1.35E-02	747	596	584	580
3	900	348	1.50E-04	6.52E-04	505	353	349	348
4	900	216	7.10E-05	3.09E-04	479	235	218	216
5	1200	198	1.80E-06	7.83E-06	455	201	198	198
6	900	370	1.30E-03	5.65E-03	590	397	379	373
7	950	220	1.30E-04	5.65E-04	521	254	224	221
8	1250	292	6.30E-05	2.74E-04	603	307	294	292
9	1000	564	8.70E-03	3.78E-02	750	610	590	582
10	950	282	1.50E-04	6.52E-04	526	297	284	283
11	900	490	8.10E-03	3.52E-02	680	537	515	506
12	900	528	1.90E-02	8.26E-02	728	602	575	561
13	900	528	2.10E-02	9.13E-02	734	608	579	564

Table S1.4. (cont.)

Case	T_h (°C)	T_c (°C)	A_h (m ²)	p	Pixel-Integrated Temperature (°C)			
					NIR	SWIR	MIR	TIR
14	900	278	7.00E-04	3.04E-03	564	324	287	280
15	900	546	1.50E-02	6.52E-02	715	600	581	570
16	900	332	3.20E-03	1.39E-02	632	409	358	341
Mean	966	385	5.61E-03	2.44E-02	620	427	404	396
Type 2								
1	1000	262	3.90E-04	1.70E-03	587	311	270	264
2	1100	210	1.20E-04	5.22E-04	578	264	216	211
3	900	340	6.10E-06	2.65E-05	407	340	340	340
Mean	1000	271	1.72E-04	7.48E-04	524	305	275	271
Type 3								
1	900	260	5.00E-05	2.17E-04	467	266	261	260
2	900	304	3.50E-06	1.52E-05	391	304	304	304
3	950	236	2.90E-05	1.26E-04	469	243	237	236
4	950	238	3.00E-05	1.30E-04	470	245	239	238
5	1100	302	1.40E-05	6.09E-05	495	304	302	302
6	950	256	2.00E-05	8.70E-05	457	260	256	256
7	950	294	6.80E-06	2.96E-05	425	295	294	294
8	900	210	3.70E-06	1.61E-05	392	211	210	210
9	900	270	5.70E-06	2.48E-05	403	271	270	270
10	1250	280	1.40E-05	6.09E-05	540	284	280	280
11	900	208	9.40E-07	4.09E-06	358	208	208	208
12	1100	296	8.70E-06	3.78E-05	479	297	296	296
13	1150	294	2.00E-05	8.70E-05	524	298	294	294
Mean	992	265	1.59E-05	6.90E-05	451	268	266	265
All Data								
No.	32							
Min	900	198	9.40E-07	4.09E-06	358	201	198	198
Max	1250	572	2.10E-02	9.13E-02	750	610	590	582
Mean	980	326	2.83E-03	1.23E-02	542	351	336	331
St. Dev	112	115	5.73E-03	2.49E-02	116	132	127	123

During their measurements, Flynn *et al.* (1993) identified three types of activity at the lake, each of which will generate different pixel-integrated temperatures in the NIR, SWIR, MIR and TIR:

- Type 1 was characterized by lava fountaining and overturning of the crust, so that crust temperatures and crack areas were highest during this type of activity. Thus, as we see from Table S1.4, pixel-integrated temperatures were also highest for this activity type, having

typical values of around 620 °C (at 0.85 μm), 430 °C (at 2.25 μm), 405 °C (at 3.75 μm) and 395 °C (at 11 μm). Note here the effect of the integrated temperature becoming weighted towards the cooler, crusted component as we move towards the TIR, so that (for the same thermal structure) pixel-integrated temperatures decrease from the NIR to the TIR.

- Type 2 activity involved rifting events between plates of crust, with Type 3 activity being characterized by the development of thick, cooler crusts. During Type 2 and 3 activity crust temperatures and crack areas were lower, hence so, too, were pixel-integrated temperatures. However, Table S1.4 still shows pixel-integrated temperatures for such surfaces of 450 °C to 520 °C (at 0.85 μm), 270 °C to 305 °C (at 2.25 μm), and \sim 270 °C (at both 3.75 μm and 11 μm).

The lava lake pixel-integrated temperatures of Table S1.4 are plotted over the dynamic ranges of TM, AVHRR and GOES in Figure 1.3a. We see that:

- For the NIR such a surface is insufficiently radiant to be detected, the pixel-integrated temperature for all three types of activity being less than the lower limit of the sensor dynamic ranges. The one exception is TM band 4 (0.83 μm) for which Type 1 activity can produce a pixel-integrated temperature that falls within the lower end of the sensor dynamic range.
- For the SWIR there is detectable radiance, so that the pixel-integrated temperatures for all three types of activity fall within or exceed the sensor dynamic ranges. The problem is that the pixel-integrated temperatures for some cases exceed the sensor dynamic ranges. Type 1 activity will thus likely saturate the sensor at 1.65 μm , and both Type 1 and Type 2 activity will saturate at 2.22 μm .
- All three types of activity are detectable in the MIR and TIR, but the pixel-integrated temperatures exceed the upper limit of typical sensor dynamic ranges in these spectral regions. Thus, a lava lake will saturate a pixel filled by an active lava lake pixel in the MIR or TIR.

Lava lake detection in TM-class data

We have so far considered a case where the pixel is filled by the active lava source and pixel-integrated temperature is described by the two-component model of Equation S1.5. Such a case applies to TM-class data where pixels are sufficiently small to be filled by the active lava source. As a result, the above detection expectations are borne out by the two examples given in Figure S1.4, which consider TM data for lava lakes active at Pu'u 'O'o (Kilauea) and Erebus. We see that, for pixels centered over the lakes themselves, SWIR bands 5 and 7 are saturated. However, NIR bands 3 and 4 are non-responsive, the exception being the Pu'u 'O'o case where unsaturated band 4 data are available. Clearly the Pu'u 'O'o lake was extremely active. Seven of the sixteen Type 1 activity examples given in Table S1.4 result in pixel-integrated temperatures in the NIR which are greater than the lower detection limit (595 °C) of TM band 4. Thus, the lake must have been experiencing this type of activity at the time of image acquisition. From Figure S1.4 we see that TM-class data over active lava lakes are generally saturated, unless the radiance source is sufficiently intense to cause

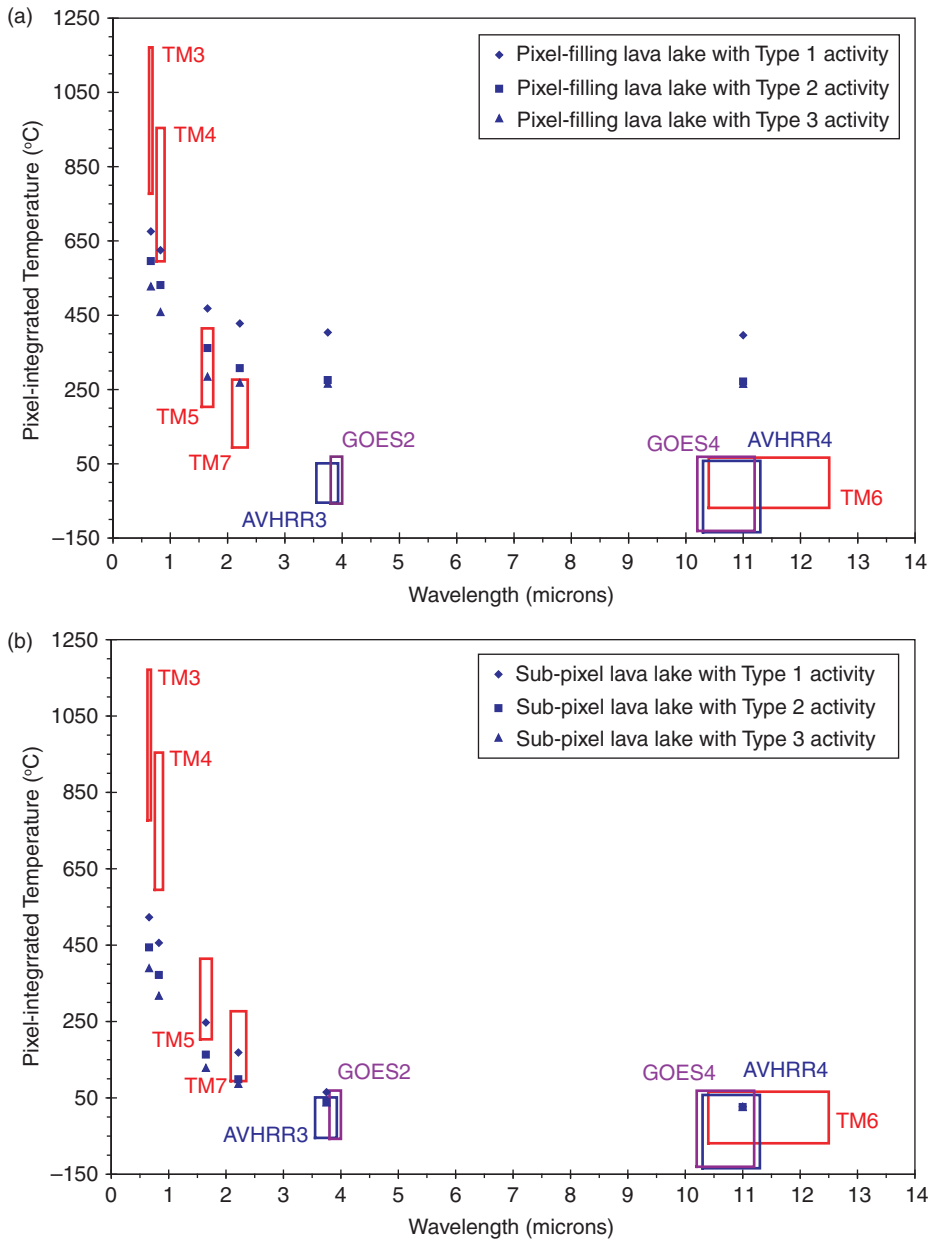


Figure S1.3 (a) Waveband and dynamic range for some selected sensors in relation to (a) the expected pixel-integrated temperatures for a pixel-filling lava lake with the thermal surface of Table S1.4, and (b) the expected pixel-integrated temperatures for a sub-pixel lava lake with the size and temperature characteristics of Table S1.5. Plots falling below a box define cases that are not detectable by the sensor; those falling above a box cause saturation; those falling within a box register measurable spectral radiance.

detectable radiance in band 4 or sufficiently stagnant so as to bring the levels of emitted radiance below the saturation limits of the SWIR and TIR bands.

Three other detection problems resulting from the intensity of the radiant source are apparent from the examples in Figure S1.4. These are:

(a)

Band 7

25	29	45	52	50	37	23	22	20	28	41	26	14	18
28	48	52	60	72	60	39	32	31	36	41	28	20	19
30	42	73	106	82	46	93	100	106	108	66	43	46	35
27	42	59	60	83	134	255	206	84	108	65	80	64	37
47	75	99	138	87	255	255	255	255	255	133	51	36	29
0	0	0	255	255	255	255	255	255	255	105	106	71	39
255	255	255	255	255	255	255	255	255	255	177	62	45	35
107	61	43	65	143	255	255	255	255	255	152	103	73	34
100	38	45	56	86	111	255	255	169	255	234	82	39	27
143	67	38	45	69	102	147	159	189	197	139	111	69	38
153	113	89	96	106	108	98	98	153	173	110	62	29	24
121	146	140	112	101	111	93	73	79	98	85	73	41	29
58	104	109	92	70	54	66	71	72	74	71	45	24	16
30	37	39	41	46	60	70	54	47	67	35	46	41	24

Band 5

24	28	38	39	50	39	27	27	27	37	75	49	22	24
35	54	64	47	48	48	42	39	43	48	63	47	29	27
35	44	64	98	87	57	53	64	69	69	64	52	59	47
40	66	89	98	74	74	128	98	54	72	54	59	59	39
58	84	104	97	91	75	255	255	207	96	71	51	37	33
187	184	201	237	255	255	255	255	255	235	59	58	50	39
0	0	0	0	0	255	255	255	255	255	64	48	33	29
143	91	43	32	45	80	209	255	255	245	89	57	42	36
138	47	31	34	39	35	133	157	41	120	102	68	32	29
201	112	44	38	42	54	76	66	90	102	84	75	58	31
204	157	96	78	93	117	89	82	91	103	85	56	33	23
149	196	189	161	118	109	85	83	80	87	78	68	37	27
79	138	139	105	88	78	79	79	76	72	64	55	32	23
48	57	62	57	59	64	77	76	67	77	59	53	42	31

Band 4

23	25	29	33	37	28	23	23	25	35	57	40	22	26
29	41	39	36	36	33	30	35	36	45	50	33	26	25
30	31	40	58	60	41	37	40	38	39	43	38	47	43
32	39	49	65	50	38	37	46	48	46	38	40	38	31
40	54	58	52	40	37	42	47	41	39	37	33	31	29
40	47	47	40	28	26	35	40	39	37	35	30	30	29
46	49	42	29	26	30	42	78	51	31	28	26	26	26
53	44	28	24	26	31	34	59	43	33	26	24	24	24
56	31	27	30	30	34	34	28	33	39	37	30	24	24
54	30	28	37	35	37	35	31	43	45	43	35	28	25
58	39	30	35	39	43	41	44	52	50	42	33	25	24
61	53	48	46	49	50	50	56	56	54	49	36	25	24
57	59	51	48	49	53	54	55	57	55	51	39	26	23
34	45	47	49	55	56	57	58	55	48	48	41	29	25

Figure S1.4 DN grids from TM images of lava lakes active at (a) Pu'u 'O'o (imaged on 23 July 1991) and (b) Erebus (imaged on 29 January 1989). Pixels are 30 m across. Marked on each are saturated pixels (red background), the hot spot area (outlined in red), sensor drop out lines (blue background) and the "halo" pixels (yellow background). Note how the decreasing sensitivity of the sensor to the sub-pixel hot spot as we move to shorter wavelengths (i.e., from band 7 to band 4) causes the degree of bleeding (i.e., the hot spot size), and number of saturated pixels, to decrease. Given the area of the Pu'u 'O'o lava lake (4000 m² or 60–70 m across), it probably occupied the three thermally anomalous pixels apparent in band 4, so that all other thermally anomalous pixels are thermally radiant due to bleeding from the high intensity pixels that actually contained the lava lake.

(b)

Band 7

25	13	16	26	30	23	26	16	11
10	21	35	100	194	125	54	23	16
29	0	255	255	255	255	129	40	16
21	73	16	255	255	255	88	24	22
24	16	21	155	146	81	58	28	11
22	18	19	22	49	37	21	15	13
30	15	12	15	18	21	33	12	9

Band 5

20	11	7	9	12	11	12	11	11
11	11	12	27	43	32	15	12	9
13	28	10	255	255	255	22	12	12
21	21	12	135	255	115	22	12	12
26	9	12	37	32	19	16	9	7
40	17	8	11	14	12	10	7	10
41	20	9	9	11	7	9	9	6

Band 4

31	21	16	14	14	14	18	23	22
28	24	15	10	9	9	10	15	20
25	20	15	9	9	9	8	11	18
31	18	14	10	10	10	10	11	14
54	22	13	11	10	10	11	11	10
87	33	17	14	11	11	11	11	12
120	68	36	15	12	12	13	14	20

Figure S1.4 (cont.)

- Radiance bleeding – This is caused by spreading of radiance into pixels where the radiance does not belong due to pixel overlap and the point spread function. In the cases given in Figure S1.4 this has caused radiance to spread up to three pixels beyond the pixel actually containing the lava lake.
- Sensor recovery (sensor drop out) – Down scan of the most intense radiance source the sensor becomes jammed and records saturated or minimum value radiances (DN = 0 or 255) for several pixels down scan of the hot spot.

- Hot spot halos – Reflection of radiance within the instrument telescope causes a halo of radiant pixels around, but detached from, the hot spot itself. In the case of the Pu'u 'O'o example in Figure S1.4a the halo is located down scan and down track of the hot spot. Note that the image was acquired during descending mode, so the track was from north-to-south.

Lava lake detection in AVHRR- and GOES-class data

For TM-class data, the lava lake typically fills the pixel so that the Equation (S1.5) model applies. Lava lakes are, however, typically 10s to 100s of meters in width. The Kupaianaha lava lake considered by Flynn *et al.* (1993) was, for example, 50 m wide with an area of 2300 m² at the time of measurement. Thus a lava lake will typically be smaller than the pixel in one-to-four kilometer AVHRR- and GOES-class data, so that the lava lake itself will be a sub-pixel feature. In this case, the three-component model of Equation (S1.6) needs to be applied to obtain the pixel-integrated temperature. The relegation of the lava lake to a sub-pixel feature and inclusion of surrounding ground at ambient temperatures means that the lava lake is less likely to saturate the sensor. To test this, we can use Equation (S1.6) to estimate the pixel-integrated radiance for a 2300 m² lake centered in a 1 km² pixel. First, we need to estimate the crack (A_{crack}) and crust (A_{crust}) area. This can be done using the lake area (A_{lake}) in

$$A_{\text{crack}} = p A_{\text{lake}} \quad (\text{S1.7a})$$

and

$$A_{\text{crust}} = (1 - p) A_{\text{lake}} \quad (\text{S1.7b})$$

Using the mean values for Type 1 activity in Table S1.4 we obtain

$$A_{\text{crack}} = (2.44 \times 10^{-2})(2300 \text{ m}^2) = 56.1 \text{ m}^2$$

and

$$A_{\text{crust}} = (1 - 2.44 \times 10^{-2})(2300 \text{ m}^2) = (9.76 \times 10^{-1})(2300 \text{ m}^2) = 2243.9 \text{ m}^2$$

Equations (S1.5b) and (S1.6b) can next be used to estimate the portion of the pixel occupied by crack (p) and crust (p_c) components:

$$p = 56.1 \text{ m}^2 / 1\,000\,000 \text{ m}^2 = 5.61 \times 10^{-5}$$

and

$$p_c = 2243.9 \text{ m}^2 / 1\,000\,000 \text{ m}^2 = 2.24 \times 10^{-3}$$

We can then use these values to estimate the pixel-integrated radiance in Equation (S1.6a). Here we consider the pixel-integrated radiance in the MIR ($\lambda = 3.75 \mu\text{m}$) and solve Equation

(S1.6a) using the spectral radiance equivalents of the mean crack and crust temperatures for Type 1 activity as given in Table S1.4, along with an assumed ambient ground temperature of 25 °C. This yields:

$$\begin{aligned}
 M(\lambda, T_{\text{int}}) &= (5.61 \times 10^{-5})M(3.75 \mu\text{m}, 966 \text{ }^\circ\text{C}) + (2.24 \times 10^{-3})M(3.75 \mu\text{m}, 385 \text{ }^\circ\text{C}) \\
 &\quad + (1 - 5.61 \times 10^{-5} - 2.24 \times 10^{-3})M(3.75 \mu\text{m}, 25 \text{ }^\circ\text{C}) \\
 &= (5.61 \times 10^{-5}) (2.38 \times 10^{10} \text{ W m}^{-2}\text{m}^{-1}) + (2.24 \times 10^{-3}) \\
 &\quad (1.49 \times 10^9 \text{ W m}^{-2}\text{m}^{-1}) + (0.99986) (1.29 \times 10^6 \text{ W m}^{-2}\text{m}^{-1}) \\
 &= 5.97 \times 10^6 \text{ W m}^{-2}\text{m}^{-1}
 \end{aligned}$$

By using the inversion of the Planck Function as given in Equation (2.5) of Chapter 2 we find that this pixel-integrated radiance converts to a pixel-integrated temperature of 65 °C. Thus, the inclusion of a large area of ambient ground within the pixel brings the pixel-integrated temperature down to around the upper-bound of the dynamic range for sensors operating in the MIR (i.e., 50 to 60 °C).

In Table S1.5 we follow the above steps to estimate the pixel-integrated temperatures in the NIR, SWIR, MIR and TIR for all three types of activity at a 2300 m² lava lake centered in a 1 km² AVHRR pixel and a 16 km² GOES pixel. These results are plotted over the typical NIR, SWIR, MIR and TIR sensor dynamic ranges in Figure S1.3b. We see that:

Table S1.5. *Pixel-integrated temperatures in the NIR ($\lambda = 0.85 \mu\text{m}$), SWIR ($\lambda = 2.25 \mu\text{m}$), MIR ($\lambda = 3.75 \mu\text{m}$) and TIR ($\lambda = 11 \mu\text{m}$) for a 2300 m² lava lake centered in (1) a 1 km² AVHRR-class pixel, and (2) a 16 km² GOES-class pixel. Pixel-integrated temperatures are calculated using the mean crack and crust temperature (T_h and T_c) and hot crack portion (p) values for Type 1, 2 and 3 activity given in Table S1.4, with an ambient temperature (T_a) of 25 °C.*

Case	A_h (m ²)	A_c (m ²)	p	p_c	Pixel-Integrated Temperature (°C)			
					NIR	SWIR	MIR	TIR
(1) 1 km ² AVHRR Pixel ($A_{\text{pixel}} = 1\,000\,000 \text{ m}^2$, $A_{\text{lake}} = 2300 \text{ m}^2$)								
Type 1	56.10	2243.90	5.61E-05	2.24E-03	449	165	65.2	26.9
Type 2	1.72	2298.28	1.72E-06	2.30E-03	364	96	39.3	26.1
Type 3	0.16	2299.84	1.59E-07	2.30E-03	310	85	38.1	26.0
(2) 16 km ² GOES Pixel ($A_{\text{pixel}} = 16\,000\,000 \text{ m}^2$, $A_{\text{lake}} = 2300 \text{ m}^2$)								
Type 1	56.10	2243.90	3.51E-06	1.40E-04	372	96	29.8	25.1
Type 2	1.72	2298.28	1.08E-07	1.44E-04	304	49	26.1	25.1
Type 3	0.16	2299.84	9.92E-09	1.44E-04	259	42	26.0	25.1

- For the NIR such a sub-pixel hot spot is insufficiently radiant to be detected, the pixel-integrated temperature for all three types of activity being less than the lower limit of the sensor dynamic ranges.
- For the SWIR there is a detectable radiance only for Type 1 activity.
- All three types of activity fall within the sensor dynamic ranges in the MIR and TIR, and are thus detectable and will not saturate the sensor.

In short, size of the hot source (lava lake) is too small to attain detectable radiance levels in the NIR and SWIR, although an extremely active (Type 1) lake may be detectable in a 1 km² SWIR pixel (but not in a 16 km² SWIR pixel). In the MIR and TIR, the lake is detectable and does not saturate either the 1 km² or the 16 km² pixel (although a large lake undergoing Type 1 activity may saturate the MIR).

The problem is, the radiance contribution of the lava lake may be so small in the MIR and TIR that it does not elevate the pixel-integrated temperature sufficiently above the background to be detectable. From Table S1.5 we see that, for AVHRR-class data:

- In the MIR, the pixel-integrated temperature is elevated by at least 8 °C above the background temperature (25 °C) for all types of activity.
- In the TIR, the pixel-integrated temperature is elevated by just 1.9 °C for Type 1 activity, and ~1 °C for Type 2 and Type 3 activity.

For GOES-class data:

- In the MIR, the pixel-integrated temperature is elevated by just 4.8 °C for Type 1 activity, and ~1 °C for Type 2 and Type 3 activity.
- In the TIR, the pixel-integrated temperature is elevated by just 0.1 °C for all types of activity.

Thus, such a lava lake will only have a resolvable anomaly in the MIR of AVHRR-class data. A lava lake will be resolvable in the MIR of GOES-class data and TIR of AVHRR-class data only if the lava lake is sufficiently large and/or active. We can illustrate these detection issues using AVHRR brightness temperature transects across the lava lake active at Mt. Erebus (Antarctica) in 1980. These are given in Figure S1.5. We see that the lava lake causes the MIR (band 3) brightness temperature to become elevated by at least 60 °C above the (very cold) background to saturate the sensor. In the TIR, the anomaly is more subtle, being elevated by just a few degrees centigrade above the background.

Two other detection problems resulting from the intensity of the radiant source in the MIR are apparent from Figure S1.5:

- Radiance bleeding – The lava lake at Erebus had dimensions of just 60 m by 40 m in January 1978. Thus, the hot spot from this source should fall within a single 1 km AVHRR pixel. However, the transects of Figure S1.5 show that up to four pixels are affected in the scan direction, meaning that radiance is being spread into at least one pixel in both the up- and down-scan directions.

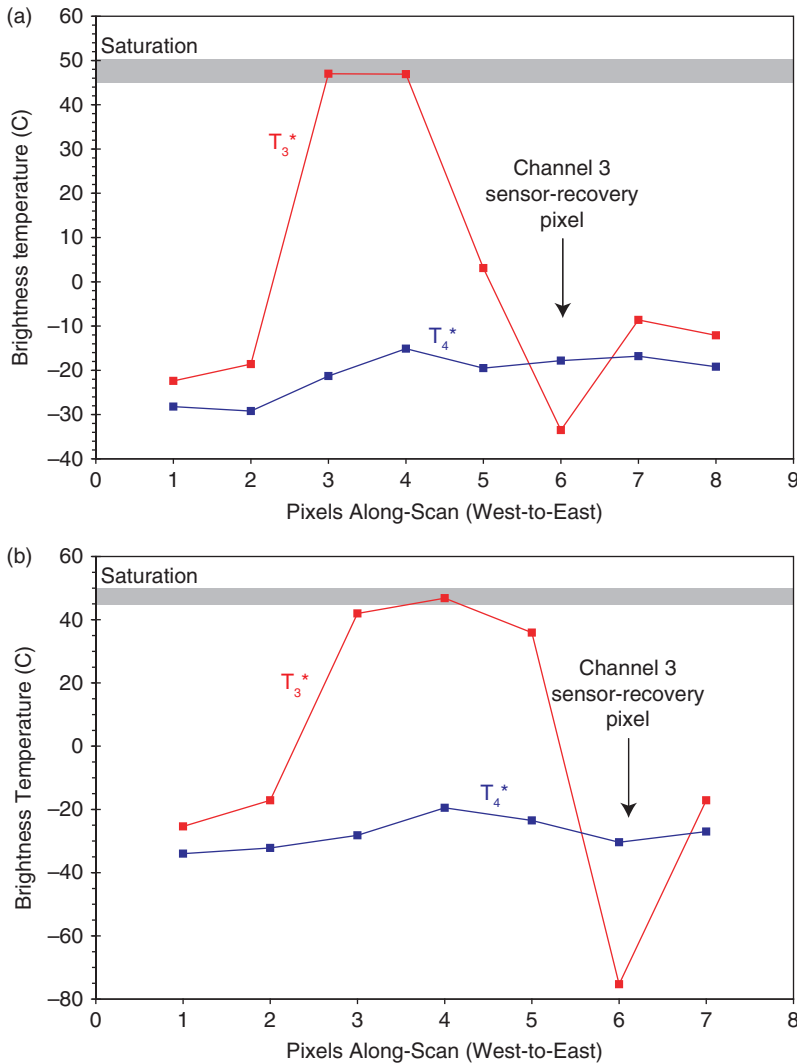


Figure S1.5 AVHRR brightness temperature transects in the MIR and TIR (T_3^* and T_4^*) taken across two AVHRR images of Erebus' lava lake acquired on (a) 13 January 1980 at 16:32Z and (b) 29 November 1980 at 07:50Z. Pixel diameters are 1.1 km in both images, compared with lava lake dimensions of 100 m \times 60 m. Note the low background temperatures in this Antarctic environment, as well as the anomalously low (sensor recovery) value immediately down-scan of the hot spot in the MIR band (channel 3). T_3^* is saturated and suffers bleeding into at least one along-scan pixel, instead T_4^* shows a subtle, one-pixel anomaly (which is about what we expect given the lake size).

- Sensor recovery – In AVHRR's MIR band the presence of an intense radiance source often causes a down-scan sensor response whereby an anomalously low radiance is recorded for one or two pixels immediately down-scan of the anomaly. This is apparent in the transects given here where the effect results in brightness temperatures as low

as $-80\text{ }^{\circ}\text{C}$ just down-scan of the anomaly, compared with typical temperatures for pixels surrounding the hot spot of around $-20\text{ }^{\circ}\text{C}$.

S1.3.2 Thermal structures and detection of active channels

The size and temperature of the thermal components that comprise the surface of an active lava channel have been estimated by Flynn and Mouginiis-Mark (1994) using spectroradiometer data obtained at Kilauea during February 1992. Their results are given in Table S1.6 along with the pixel-integrated temperatures that these yield in the NIR, SWIR, MIR and TIR – if the channel surface fills the pixel.

Flynn and Mouginiis-Mark (1994) identified two thermal zones on the channel surface each of which will generate different pixel-integrated temperatures in the NIR, SWIR, MIR and TIR:

- Zone 1 – Channel center. This was characterized by high crust temperatures and crack areas. Thus, as we see from Table S1.6, pixel-integrated temperatures are also highest for the channel center, having typical values of around $1000\text{ }^{\circ}\text{C}$ (at $0.85\text{ }\mu\text{m}$), $960\text{ }^{\circ}\text{C}$ (at $2.25\text{ }\mu\text{m}$), $950\text{ }^{\circ}\text{C}$ (at $3.75\text{ }\mu\text{m}$) and $940\text{ }^{\circ}\text{C}$ (at $11\text{ }\mu\text{m}$). Note, again, the effect of the pixel-integrated temperature becoming weighted towards the cooler, crusted component as we move towards the TIR. However, in this case, high crust temperatures and crack areas mean that pixel-integrated temperatures remain above $900\text{ }^{\circ}\text{C}$ even in the TIR.
- Zone 2 – Channel Margins. Crust temperatures and crack areas were lower at the channel margins. Table S1.6 thus shows that pixel-integrated temperatures for channels with Zone 2 thermal properties will be around $650\text{ }^{\circ}\text{C}$ (at $0.85\text{ }\mu\text{m}$), $430\text{ }^{\circ}\text{C}$ (at $2.25\text{ }\mu\text{m}$), $380\text{ }^{\circ}\text{C}$ (at $3.75\text{ }\mu\text{m}$) and $360\text{ }^{\circ}\text{C}$ (at $11\text{ }\mu\text{m}$).

All of these pixel-integrated temperatures exceed the dynamic ranges of all current sensors operating in the SWIR, MIR and TIR. This is plain from Figure S1.6 where the lava channel pixel-integrated temperatures of Table S1.6 are plotted over the dynamic ranges of TM, AVHRR and GOES. For all SWIR, MIR and TIR bands, the pixel-integrated temperatures are vastly in excess of the upper limit of the dynamic range so that, although such a pixel-filling surface will be easy to detect, data at all wavelengths will be saturated. The exception is in the NIR where the range of pixel-integrated temperatures fall within the sensor dynamic ranges so that the hot spot will (for most cases) be detectable and provide unsaturated data.

Lava channel detection in TM-class data

Although a 5 to 20 m wide channel may only partially fill a 30 m wide TM-class pixel, the temperature of an active channel surface means that emission will be intense at all wavelengths. The above detection expectations are thus born out by the example given in Figure S1.7, which is an ETM+ image of a lava channel active on Etna in October 1999. We see that, for pixels centered over the bifurcated channel, SWIR bands 5 and 7 are saturated, and

Table S1.6. Lava channel hot crack temperature and area, as well as crust temperature, from Table 1 of Flynn and Mougini-Mark (1994). Area of the surface occupied by the crack component is calculated from p using Equation (S1.5b) and the A_{pixel} of 18 m^2 given by Flynn and Mougini-Mark (1994). Temperature data were converted to radiances in the NIR ($\lambda = 0.85 \mu\text{m}$), SWIR ($\lambda = 2.25 \mu\text{m}$), MIR ($\lambda = 3.75 \mu\text{m}$) and TIR ($\lambda = 11 \mu\text{m}$) using the Planck Function [Equation (2.4) of Chapter 2]. Pixel-integrated radiances in the NIR, SWIR, MIR and TIR can then be calculated using Equation (S1.5a). Finally, pixel-integrated radiance is converted to temperature by using the inversion of the Planck Function as given in Equation (2.5) of Chapter 2.

Case	T_h (°C)	T_c (°C)	A_h (m ²)	p	Pixel-Integrated Temperature (°C)			
					NIR	SWIR	MIR	TIR
Channel Center								
1	1130	736	1.98	0.11	919	811	791	781
2	1150	928	5.58	0.31	1045	1010	1002	998
3	1120	940	10.80	0.60	1075	1056	1052	1048
4	1090	870	7.20	0.40	1009	973	965	959
5	1100	876	5.94	0.33	1003	965	956	951
6	1100	880	5.22	0.29	994	957	949	945
7	1120	870	4.86	0.27	1001	954	945	938
8	1120	872	3.96	0.22	987	941	933	927
Mean	1116	872	5.69	0.32	1004	958	949	943
Channel Margin								
9	900	400	0.11	5.90E-03	592	421	407	403
10	1100	572	0.14	7.50E-03	713	586	579	576
11	900	348	0.22	1.20E-02	625	409	368	356
12	900	216	0.16	9.00E-03	611	360	259	224
13	1200	198	0.15	8.20E-03	766	428	278	210
14	900	370	0.11	6.00E-03	593	399	379	374
Mean	983	351	0.15	8.10E-03	650	434	378	357
All Data								
No.	14							
Min	900	198	1.06E-01	5.90E-03	592	360	259	210
Max	1200	940	1.08E+01	6.00E-01	1075	1056	1052	1048
Mean	1059	648	3.32E+00	1.84E-01	852	734	705	692
St. Dev	108	284	3.42E+00	1.90E-01	190	279	306	317

there is detectable radiance in NIR band 4 along the line of the channel. We also see that the intensity of the of the emission causes widespread bleeding. Bleeding is particularly extreme in SWIR band 7 and causes the red blur witnessed around the core of the anomaly apparent in Figure S1.7.

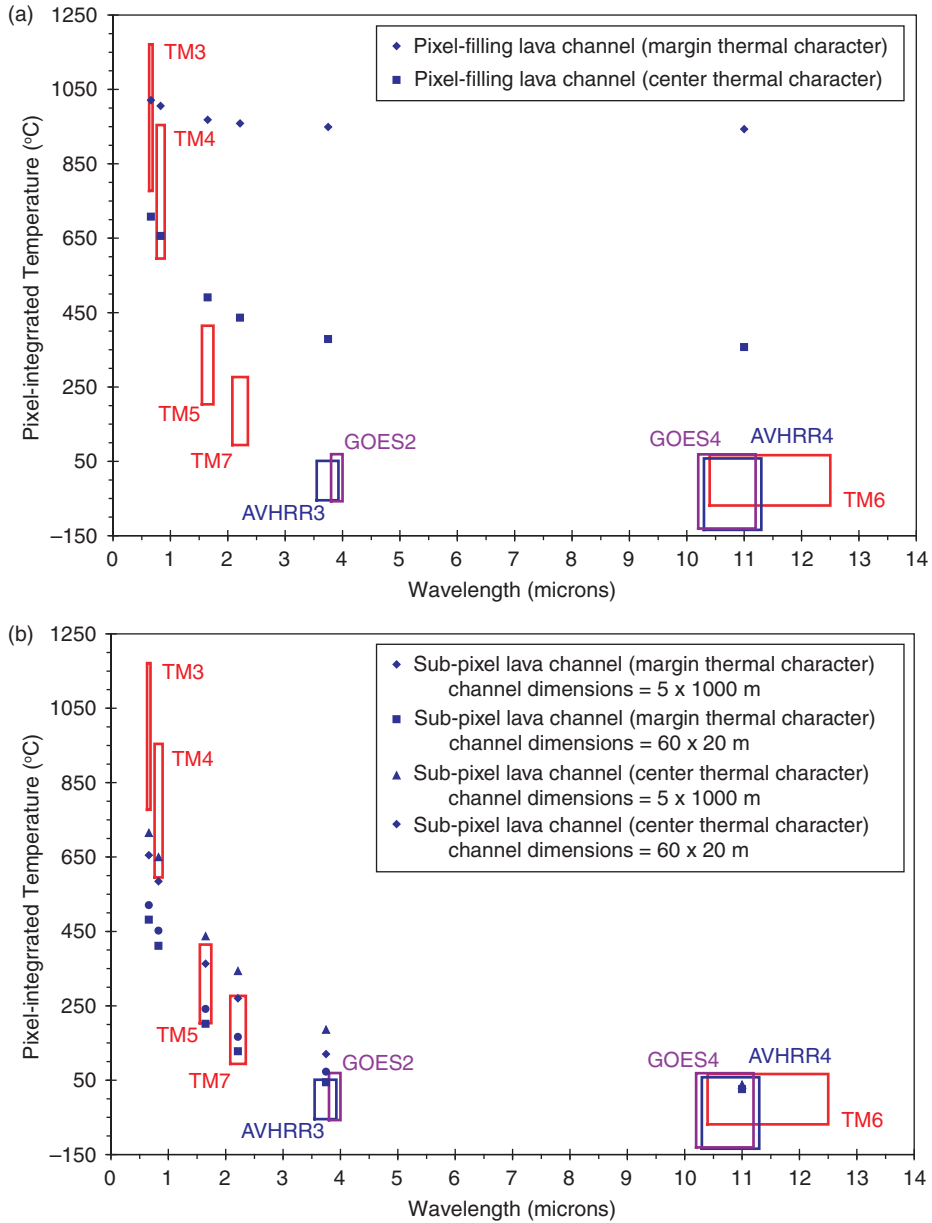


Figure S1.6 (a) Waveband and dynamic range for some selected sensors in relation to (a) the expected pixel-integrated temperatures for a pixel-filling lava channel with the thermal surface of Table S1.6, and (b) the expected pixel-integrated temperatures for a sub-pixel lava channel with the size and temperature characteristics of Table S1.7. Plots falling below a box will define cases that are not detectable by the sensor; those falling above a box will cause saturation; those falling within a box will register a measurable spectral radiance.

Table S1.7. *Pixel-integrated temperatures in the NIR ($\lambda = 0.85 \mu\text{m}$), SWIR ($\lambda = 2.25 \mu\text{m}$), MIR ($\lambda = 3.75 \mu\text{m}$) and TIR ($\lambda = 11 \mu\text{m}$) for an active lava channel centered in (1) a 1 km^2 AVHRR-class pixel, and (2) a 16 km^2 GOES-class pixel. Pixel-integrated temperatures are calculated using the mean crack and crust temperature (T_h and T_c) and hot crack portion (p) values for the channel center and margin cases given in Table S1.6, with an ambient temperature (T_a) of $25 \text{ }^\circ\text{C}$. We consider three lava channels: the first has the dimensions of the channel measured by Flynn and Mouginiis-Mark (1994), i.e., it is 60 m long and 20 m wide, the second is 5 m wide but extends right across an AVHRR pixel (i.e., it is 1 km long). We also consider a 10 m wide channel that extends right across a GOES pixel (i.e., the channel is 4 km long). In the AVHRR case this third channel will extend over four 1 km pixels, so we use a $10 \text{ m} \times 1000 \text{ m}$ dimension.*

Case	$A_h \text{ (m}^2\text{)}$	$A_c \text{ (m}^2\text{)}$	p	p_c	Pixel-Integrated Temperature ($^\circ\text{C}$)			
					NIR	SWIR	MIR	TIR
Channel Dimension: 20 m wide \times 60 m long								
(1) 1 km^2 AVHRR Pixel ($A_{\text{pixel}} = 1\,000\,000 \text{ m}^2$, $A_{\text{lake}} = 1200 \text{ m}^2$)								
Center	379.50	820.50	3.80E-04	8.21E-04	577	265	120.2	28.2
Margin	9.72	1190.28	9.72E-06	1.19E-03	404	124	44.2	25.8
(2) 4 km^2 GOES Pixel ($A_{\text{pixel}} = 16\,000\,000 \text{ m}^2$, $A_{\text{lake}} = 1200 \text{ m}^2$)								
Center	379.50	820.50	2.37E-05	5.13E-05	473	163	46.2	25.2
Margin	9.72	1190.28	6.08E-07	7.44E-05	336	67	26.7	25.1
Channel Dimension: 5 m wide \times 1000 m long								
(1) 1 km^2 AVHRR Pixel ($A_{\text{pixel}} = 1\,000\,000 \text{ m}^2$, $A_{\text{lake}} = 5000 \text{ m}^2$)								
Center	1581.25	3418.75	1.58E-03	3.42E-03	643	339	185.7	37.9
Margin	40.50	4959.50	4.05E-05	4.96E-03	445	163	72.7	28.4
(2) 4 km^2 GOES Pixel ($A_{\text{pixel}} = 16\,000\,000 \text{ m}^2$, $A_{\text{lake}} = 5000 \text{ m}^2$)								
Center	1581.25	3418.75	9.88E-05	2.14E-04	523	210	76.3	25.8
Margin	40.50	4959.50	2.53E-06	3.10E-04	369	94	31.3	25.2
Channel Dimension: 10 m wide \times 4000 m long								
(1) 1 km^2 AVHRR Pixel ($A_{\text{pixel}} = 1\,000\,000 \text{ m}^2$, $A_{\text{lake}} = 10\,000 \text{ m}^2$)								
Center	3162.50	6837.50	3.16E-03	6.84E-03	678	382	226.8	49.7
Margin	81.00	9919.00	8.10E-05	9.92E-03	466	185	92.6	31.8
(2) 4 km^2 GOES Pixel ($A_{\text{pixel}} = 16\,000\,000 \text{ m}^2$, $A_{\text{lake}} = 40\,000 \text{ m}^2$)								
Center	12650.00	27350.00	7.91E-04	1.71E-03	610	301	151.1	31.6
Margin	324.00	39676.00	2.03E-05	2.48E-03	424	143	56.7	26.7

Lava channel detection in AVHRR- and GOES-class data

As with the lava lake case, as the pixel becomes larger so the inclusion of ground at ambient temperatures surrounding the lava channel brings the pixel-integrated temperature downwards. The channel examined by Flynn and Mouginiis-Mark (1994), for example, was 60 m

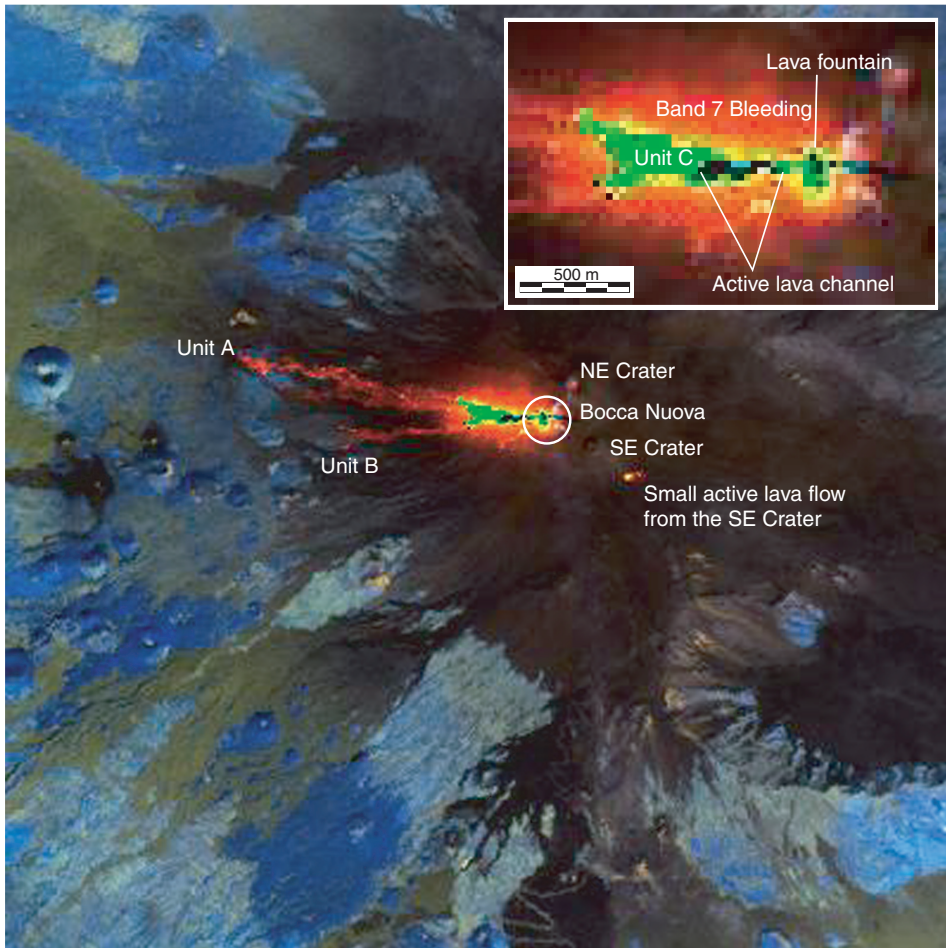


Figure S1.7 Landsat 7 ETM+ false-color composite of the summit region of Mount Etna acquired on 28 October 1999, where bands 7 (SWIR, 2.09– 2.35 μm), 5 (SWIR, 1.55– 1.75 μm), 4 (NIR, 0.75– 0.90 μm) are displayed in red, green, and blue, respectively. Over ambient surfaces reflection dominates with the reflective properties of vegetated surfaces making them blue, and barren inactive lava is black. Over the active lava thermal emission dominates, giving red if there is emission in band 7 only, yellow if there is emission in bands 5 and 7, and green-black if there is emission in all three bands. While cooler, recently inactive, lava flows (units A and B) are red, active (fountain-fed) lava flows are yellow and green (unit C, enlarged top right). The black pixels central to the unit C thermal anomaly are aligned along an active lava channel, and clustered over the active vent where a lava fountain is active (as labeled). Bleeding around the hot spot caused by active unit C causes the associated anomaly to be blurred. Because bleeding affects the most sensitive band (band 7) we see the effect as a red haze around unit C. Radiant emission from the inactive, cooling units A and B is not as intense, so we see (i) emission only in band 7, and (ii) no bleeding at these anomalies. See Wright *et al.* (2001) for a detailed description of the image and associated activity.

long and 20 m wide, for an area of 1200 m². It would thus account for just 0.12 % of the total area of a 1 km² AVHRR-class pixel and 0.0075 % of a 16 km² GOES-class pixel. In Table S1.7 we estimate the pixel-integrated temperatures in the NIR, SWIR, MIR and TIR for such a sub-pixel source in AVHRR- and GOES-class pixels for three cases:

- (1) A channel 20 m wide and 60 m long.
- (2) A 5 m wide channel extending across the full width of an AVHRR pixel.
- (3) A 10 m wide channel extending across the full width of a GOES pixel.

If we look down each column of Table S1.7, the size of the anomaly increases from case to case so that the calculated pixel-integrated temperature increases as we move down the table. We also see that the pixel-integrated temperature will always be higher for the AVHRR-class sensor than for the GOES-class sensor, a result of the lava channel taking up a greater proportion of the smaller AVHRR-class pixel. In some cases this means that the measurement for the GOES-class pixel will not be saturated when that using the AVHRR-class pixel is. For example, if we take the channel-center conditions of case (1) in Table S1.7 we expect a pixel-integrated temperature in the MIR of an AVHRR-class pixel of ~120 °C. This will saturate the sensor. For the GOES-class MIR sensor we expect a pixel-integrated temperature of ~45 °C. This will not saturate the sensor. Of course, the pixel-integrated temperatures are also higher for a channel with the high temperature characteristics of the channel center case than for the lower temperature characteristics of the channel margin case. As a result, a channel with the thermal character of the channel margin may not cause saturation. If we now take the channel-margin conditions of case (1) in Table S1.7 we expect pixel-integrated temperatures in the MIR of 44 °C and 27 °C for AVHRR- and GOES-class pixels, respectively. Finally, as we move from the NIR to the TIR the sensor becomes less sensitive to the sub-pixel hot spot, so that the recorded pixel-integrated temperature declines as we move across each row of Table S1.7. If we return to the channel-center conditions of case (1) in Table S1.7, for example, this means that although pixel-integrated temperatures are high enough (~120 °C) to saturate the MIR, they are below saturation (~28 °C) in the TIR. Thus, we may record unsaturated data in the TIR over an active lava channel.

The results of Table S1.7, for AVHRR-class pixels, are plotted over the typical NIR, SWIR, MIR and TIR sensor dynamic ranges in Figure S1.6b. We see that:

- For the NIR such a sub-pixel hot spot is sufficiently radiant to be detected in AVHRR-class data only if a channel with the thermal character of the channel center (i.e., very high crust temperature and crack areas) extends right across the pixel. Detection is unlikely in the larger GOES pixel where the smaller proportional coverage by the 1000 m × 5 m channel source results in a pixel-integrated temperature in the NIR of ~400 °C, as opposed to ~580 °C in the AVHRR-class pixel. However, a hot, wide channel extending right the way across the GOES-class pixel may be detectable, where Table S1.7 predicts a pixel-integrated temperature of ~600 °C for such a source.

- For the SWIR, radiance emitted by the channel is sufficiently intense that there is detectable radiance for all AVHRR-class cases. Table S1.7 shows that pixel-integrated temperatures for GOES-class pixels of at least 70 °C to 90 °C are to be expected. This might be just sufficient to attain the minimum detection levels of a SWIR sensor.
- For the MIR, short, narrow channels with the cooler surface character of the channel margin case may not saturate the sensor (plotting just below the upper limit of the MIR dynamic range). However, for all other cases saturation is expected. The lower pixel-integrated temperatures experienced by the GOES-class pixels mean that data are not saturated in any of the GOES-class cases considered in Table S1.7.
- For the TIR, all cases are detectable and will not saturate the sensor. As for lava lakes, the problem in the TIR is that, if the channel area is small and/or the surface too cool, the radiant contribution from the sub-pixel hot source may be so small that it does not elevate the pixel-integrated temperature sufficiently above the background to be detectable. We see this in Table S1.7 where, in some cases, the sub-pixel presence of the lava channel only elevates the pixel-integrated temperature by a few tenths of a degree above the 25 °C background.

Lava channels are sufficiently hot to be detectable in the SWIR, MIR and TIR bands of AVHRR- and GOES-class data. If the channel is sufficiently long, it may also be detectable in the NIR for AVHRR-class data. Data will be saturated in the MIR for AVHRR-class pixels, but the larger GOES-class pixel may yield unsaturated data in the MIR.

We will further examine detection issues for active lava flows when we consider the emission from the pahoehoe and 'a'a lava flow field that the channels feed and which will also be present in the larger AVHRR or GOES pixel. The problem is that, in one to four kilometer pixels, it is impossible to isolate the channel from the lava flows that it feeds, so both sources often contribute to the pixel-integrated radiance.

S1.3.3 Thermal structures and detection of active lava tubes

Thermal emission from lava flowing in a tube is shielded from the satellite-view by the tube roof. Heat conducted across the roof to the surface can cause elevated surface temperatures above the tube. However, the heating effect for mature tubes with thick roofs is often minimal, with temperatures being elevated above typical ambient levels by a few degrees to a few 10s of degrees centigrade. Observations of tubes active on Kilauea show surface temperatures typically in the range of 60 °C to 80 °C extending across zones a few 10s of meters wide and following the line of the tube. These are apparent as zones of steaming after periods of rain fall (Keszthelyi, 1995). Other sources of heat may be enhanced thermal emission from cracks in the lava flow field above the tube, but such zones are typically small (cracks and holes just a few centimeters across) with temperatures of 100 to 300 °C (Witter and Harris, 2007).

Such a source will only be detectable in the MIR and TIR. It is simply too cool to give detectable emission in the NIR and SWIR. Because lava tubes and the subtle surface thermal anomalies that mark them are typically just a few meters to tens of meters wide, these small, cool surfaces will be unresolvable in an AVHRR- or GOES-class MIR or TIR pixel. However, subtle thermal anomalies due to the presence of active lava tubes have been identified in the TIR bands of TM-class data, in which they are apparent as sinuous lines of TIR pixels elevated by a few degrees centigrade above the ambient pixels surrounding them.

Occasionally, lava flowing in the tube may be visible at holes in the roof known as skylights. At these locations the surface of the lava flowing in the tube is more or less uncrusted and thus at a very high temperature; measurements by Witter and Harris (2007) at skylights on Kilauea yielded lava surface temperatures of between 1017 °C and 1132 °C. Such a high temperature source will be detectable in the NIR, SWIR, MIR and TIR, likely saturating the SWIR, MIR and TIR. However, skylights are also typically small, being just a meter or so across. As a result, skylights are typically sub-pixel features even in TM-class pixels. In Table S1.8 we calculate the pixel portion occupied by two end member skylight cases, one being a 1 m wide skylight with a temperature of 1000 °C (case 1), the second being 5 m wide with a temperature of 1150 °C (case 2). In both cases, the ambient ground surrounding the skylight is at 25 °C. For the TM-class pixel, we see that pixel-integrated temperatures will fall within the dynamic range for most sensors, although the smaller case (case 1) may not be detectable in the NIR and the larger case (case 2) will likely saturate the SWIR and MIR. In addition, the smaller case may result in a pixel-integrated temperature that is elevated by just a few degrees Centigrade above the background. As a result, the locations of the skylights in the Figure 6.2 of Chapter 6 Tm image example are apparent as warm spots along the line of the tube.

For the AVHRR-class pixel we see that:

- Neither case will attain the lower threshold for detection in the NIR (~780 °C).
- Case 2 exceeds the typical lower threshold for detection in the SWIR (~100 °C), but case 1 does not.
- Case 2 will elevate the pixel-integrated temperature in the MIR by 13 °C above the background, but case 1 will elevate the pixel-integrated temperature by just 0.5 °C.
- Neither case is resolvable in the TIR.

For the GOES-class pixel we see that:

- Neither case will attain the lower threshold for detection in the NIR or the SWIR.
- Neither case is resolvable in the MIR or TIR.

In other words, in a GOES-class pixel the size of the hot spot is too small to contribute sufficient radiance to the pixel-integrated value.

Table S1.8. Pixel-integrated temperatures in the NIR ($\lambda = 0.85 \mu\text{m}$), SWIR ($\lambda = 2.25 \mu\text{m}$), MIR ($\lambda = 3.75 \mu\text{m}$) and TIR ($\lambda = 11 \mu\text{m}$) for a skylight centered in (1) a 30 m TM-class pixel, (2) a 1 km AVHRR-class pixel, and (3) a 4 km GOES-class pixel. In case 1, lava with a surface temperature of 1000 °C is flowing beneath a 1 m wide skylight. In case 2, lava with a surface temperature of 1150 °C is flowing beneath a 5 m wide skylight. In both cases the background is at 25 °C.

	TM		AVHRR		GOES	
	Case 1	Case 2	Case 1	Case 2	Case 1	Case 2
Model values						
T_h (°C)	1000	1150	1000	1150	1000	1150
T_a (°C)	25	25	25	25	25	25
Skylight width (m)	1	5	1	5	1	5
Skylight area (m ²)	1	25	1	25	1	25
Pixel dimension and skylight coverage						
Pixel Dimension (m)	30	30	1000	1000	4000	4000
Skylight pixel portion	1.11E-03	2.78E-02	1.00E-06	2.50E-05	6.25E-08	1.56E-06
Pixel-integrated temperature (°C)						
NIR	569	821	351	480	293	397
SWIR	268	520	68	151	34	86
MIR	122	345	25.5	38	25.0	26.0
TIR	28	99	25.0	25.1	25.0	25.0

S1.3.4 Thermal structures and detection of active lava flows

While the size and temperature of the thermal components that comprise the surface of an active pahoehoe flow have been estimated by Flynn and Mouginiis-Mark (1992) using spectroradiometer data obtained at Kilauea during February 1992, Flynn *et al.* (1997) gave values for the thermal structure at an 'a'a flow active on Kilauea during August 1995. Their results are given in Table S1.9 along with the pixel-integrated temperatures that these yield in the NIR, SWIR, MIR and TIR for cases where the active lava surface fills the pixel. As recognized by Flynn *et al.* (1997) the results for the pahoehoe and 'a'a lava flows are almost identical.

What we see from Table S1.9 is that the crusted component cools with time. As a result, the pixel-integrated temperature for an active lava flow will depend on the age of the crust. For example, the results of Table S1.9 predict a crust temperature of ~770 °C at time zero and a pixel-integrated temperature in the TIR of around 780 °C. After ~1 hour the crust temperature has declined to ~300 °C and the pixel-integrated temperature in the TIR to around 400 °C. Thus, with time, the pixel-integrated temperature for an active lava flow will

Table S1.9. Lava flow (pahoehoe) hot crack temperature and area, as well as crust temperature, from Table 1 of Flynn and Mouginis-Mark (1992). Also given are the same parameters calculated for an 'a'a flow surface by Flynn et al. (1997). Area of the surface occupied by the crack component is calculated from p using Equation (S1.5b) and the A_{pixel} of 0.55 m^2 given by Flynn and Mouginis-Mark (1992). Temperature data were converted to radiances in the NIR ($\lambda = 0.85 \mu\text{m}$), SWIR ($\lambda = 2.25 \mu\text{m}$), MIR ($\lambda = 3.75 \mu\text{m}$) and TIR ($\lambda = 11 \mu\text{m}$) using the Planck Function [Equation (2.4) of Chapter 2]. Pixel-integrated radiances in the NIR, SWIR, MIR and TIR can then be calculated using Equation (S1.5a). Finally, pixel-integrated radiance is converted to temperature by using the inversion of the Planck Function as given in Equation (2.5) of Chapter 2.

Time	T_h (°C)	T_c (°C)	A_h (m ²)	p	Pixel-Integrated Temperature (°C)			
					NIR	SWIR	MIR	TIR
Pahoehoe								
0	1150	768	0.020	0.036	861	793	786	782
20	900	604	0.006	0.010	643	610	608	607
21	950	626	0.008	0.014	682	636	632	631
22	1150	626	0.006	0.011	764	643	635	632
23	950	610	0.008	0.014	677	621	617	615
25	900	594	0.006	0.010	639	601	598	597
29	1100	550	0.003	0.005	690	561	555	553
32	950	544	0.008	0.014	665	561	553	550
41	900	454	0.005	0.009	612	473	462	458
49	900	454	0.004	0.008	607	471	461	458
52	900	410	0.003	0.005	585	426	416	413
54	900	514	0.002	0.004	584	519	517	516
59	900	390	0.012	0.021	652	455	416	402
Mean	965	550	0.007	0.012	666	567	558	555
'A'a								
0	1200	750	0.001	0.002	767	752	751	751
0	1200	750	0.002	0.003	774	753	752	751

decline. From Figure S1.8, where the pixel-integrated temperatures of Table S1.9 are plotted over the dynamic ranges of TM, AVHRR and GOES, we see that:

- In the NIR, the surface is sufficiently hot to be detectable upon emplacement. However, as the surface ages and cools so the emitted radiance levels drop below the sensor's lower detection limits.
- In the SWIR, MIR and TIR, levels of emitted radiance are sufficiently high to exceed the upper limit of the sensor dynamic range. Thus, all SWIR, MIR and TIR cases considered in Figure S1.8 are saturated.

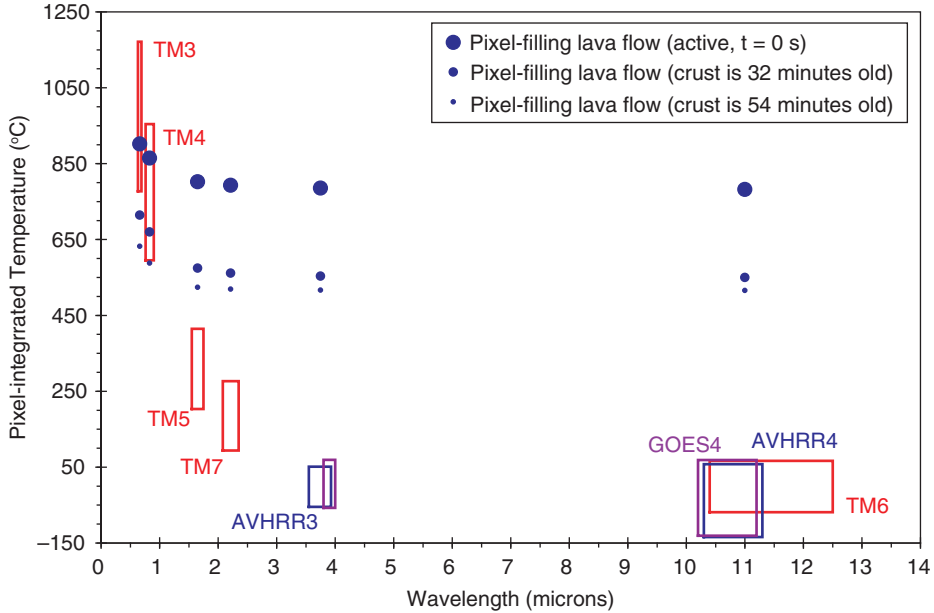


Figure S1.8 Waveband and dynamic range for some selected sensors in relation to the expected pixel-integrated temperatures for a pixel-filling lava surface of varying age (data are from Table S1.9).

We can also consider the cooling effect by plotting the expected variation in surface temperature at an active lava flow with time. Hon *et al.* (1994) used repeated radiometer temperature measurements of a cooling pahoehoe surface to define an empirical relation whereby the variation in surface temperature (T_c) with time (t , in hours) could be described by:

$$T_c = -140 \log(t) + 303 \quad (\text{S1.8})$$

In Figure S1.9 we plot this relationship for a surface composed solely of cooled crust. If we now plot the temperature limits of the various NIR, SWIR, MIR and TIR dynamic ranges we see the temperature, and therefore times, at which the surface first drops below saturation to then become undetectable. We see that:

- The surface will only saturate the NIR immediately upon exposure, and will rapidly become undetectable as the surface cools through 600 °C (this occurs within 30 seconds).
- Depending on the waveband location, the surface saturates the SWIR for between 9.5 minutes (TM-5) and 1.5 hours (TM-7). The surface becomes undetectable after 5.2 hours and 31 hours in the same two wavebands, respectively.
- In the MIR and TIR the surface will saturate the sensor for 46 hours, then become undetectable once it cools to ambient.

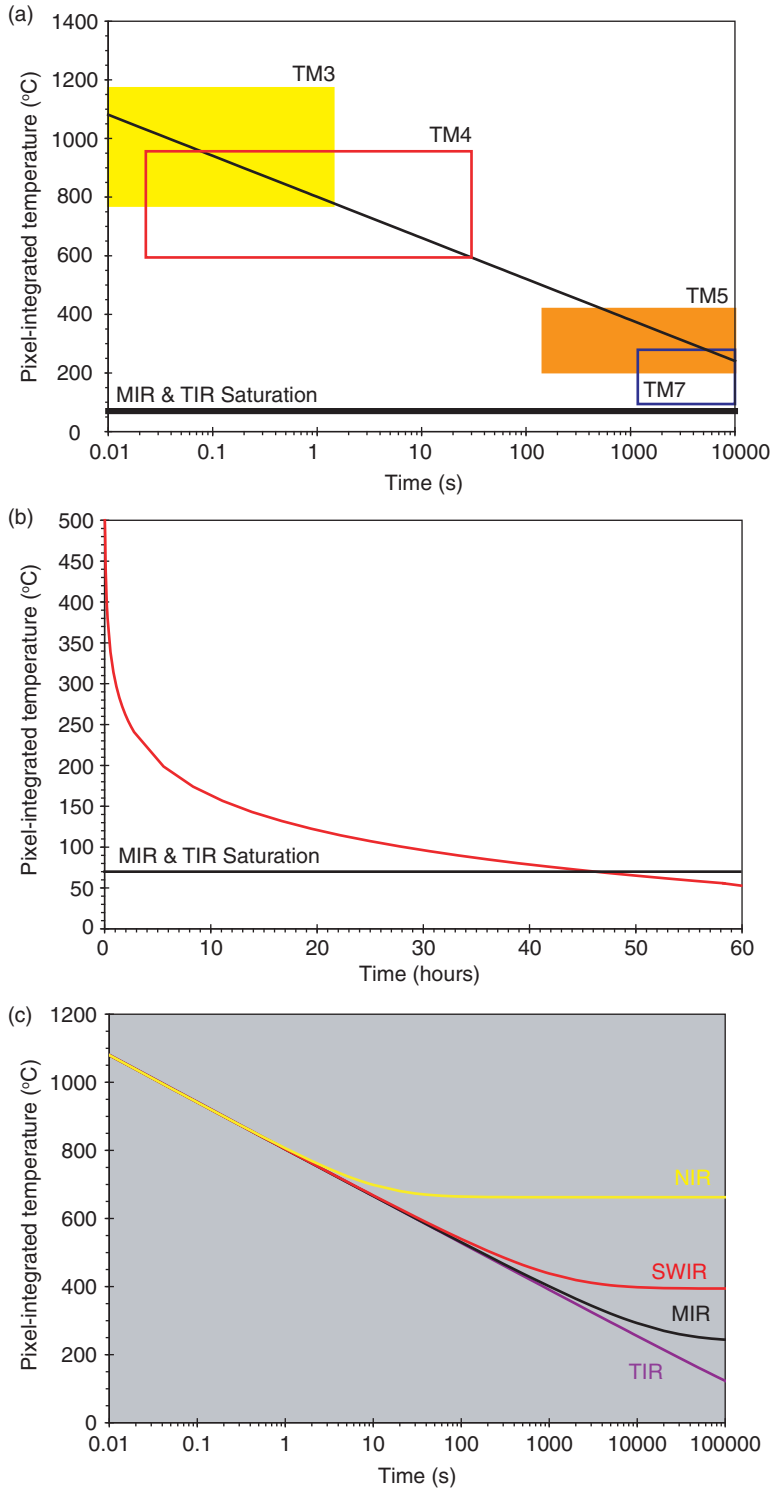


Figure S1.9 (cont.)

Thus, any active lava flow with a surface that is constantly undergoing exposure should saturate all pixels in the SWIR, MIR and TIR and should be detectable in the NIR, if the surface fills the pixel. If the surface is more than 10 minutes to 90 minutes old, it should begin to yield unsaturated data in the SWIR. The MIR and TIR should always be saturated, if the surface fills the pixel.

In Figure S1.9c we plot the pixel-integrated temperatures for a pixel occupied by a cooling crust broken by cracks with the mean properties of Table S1.9 (i.e., cracks at 965 °C occupy 1.2 % of the surface). We see that the extra radiance contribution from the hot cracks causes the pixel-integrated temperature to be elevated above the temperature expected for a pixel containing just a cooling crust at all times. Because of the different sensitivities of the different wavebands to the sub-pixel hot crack source, the effect is different for each waveband:

- For the NIR it causes the pixel-integrated temperature to attain a constant value of 663 °C after 200 seconds.
- For the SWIR it causes the pixel-integrated temperature to attain a constant value of 398 °C after 2.8 hours.
- For the MIR it causes the pixel-integrated temperature to attain a constant value of 244 °C after 28 hours.
- For the TIR, over the time scale plotted, it causes the pixel-integrated temperature to be elevated above the temperature expected for a pixel containing just a cooled crust by only a few degrees. The pixel-integrated temperature drops below saturation (70 °C) after 46 hours.

While the presence of the cracks prevents the surface from becoming undetectable in the SWIR, they ensure that the surface remains above saturation, and therefore undetectable, in the MIR.

Whether saturation occurs also depends on the area of the active lava body in relation to the area of the pixel. Figure S1.8 supports the above predictions by plotting the lava flow data of Table S1.9 with the typical sensor dynamic ranges. We see that all pixel-filling cases plot above the typical upper limits of the sensor dynamic ranges in the SWIR, MIR and TIR. The NIR is not saturated, but the surface has to be hot and recent to be detectable. If we consider a 1 or 4 km pixel with an active lava area of 100 × 500 m, the effect of the ambient background contribution will pull all pixel-integrated temperatures downwards. For such cases, we may now fall within the detection limits of the SWIR and TIR sensors. However, the MIR will likely remain saturated and the NIR unresponsive.

Caption for Figure S1.9

Figure S1.9 (a) Decrease in lava surface temperature with time, plotted through the dynamic ranges for selected sensors. (b) Decrease in lava surface temperature with time, with typical saturation levels for sensors in the MIR and TIR. (c) Decrease in pixel-integrated temperature in the NIR, SWIR, MIR and TIR for a pixel within which crust is cooling following the relation of Equation (S1.8), and is broken by cracks covering 2.1 % of the surface and at a stable temperature of 965 °C.

S1.3.5 Detection of active lava flows: Examples and problems

Active flows are sufficiently large and hot that the problem is not with detecting them, but with avoiding saturation in all classes of data, as well as spurious sensor response problems over the high intensity radiance source.

TM-class detector response over intense thermal anomalies

TM class data, having the smallest (30 to 120 m) pixels suffers the most, the hot active lava source often filling the pixel to easily attain saturation. In the example of a TM image acquired for a tube-fed pahoehoe lava flow field as given in Figure 6.2 of Chapter 6, all pixels over the core of the active lava are saturated (with DN = 255) in both the TIR (band 6) and SWIR (band 7). Only in pixels containing recently active, cooling lava are unsaturated values encountered. The same applies to the image of a channel-fed 'a'a flow active on Etna during October 1999, as given in Figure S1.7. In these examples, the case is not helped by the presence of active lava channels feeding the hot, active zones of dispersed 'a'a flow. As we already know, the channels themselves are sources of particularly intense radiance. In both cases, large areas of saturation in both SWIR bands 5 and 7 are apparent from widespread yellow colors visible at the core of the anomaly. The corollary is that such intense emission in band 7 often means measurable radiance in band 5, or in band 4 if band 5 is saturated. In the case of the October 1999 example, emission was sufficiently intense to give measurable radiance in the NIR (ETM+, band 3), apparent as the dark pixels within the yellow core of Figure S1.7.

TM-class spurious detector response over intense thermal anomalies

Two sensor response problems occur in TM data over such intense thermal anomalies: sensor recovery and radiance bleeding. Sensor recovery may be apparent as lines of corrupt data extending across and away from the anomaly (as in the lava lake example of Figure S1.4). This is a result of sensor overload over the intense anomaly, causing the sensor to lock up for a number of pixels down-scan and record a saturated value, in this case a DN of 255, in one or two of the SWIR bands. For the sake of image appearance, these corrupt lines can be cleaned up by replacement, on a pixel-by-pixel basis, with the mean DN from surrounding, non-corrupted pixels. However, the pixel data itself, for the corrupted pixels, is lost. In Figure S1.7, bleeding is also apparent from a red haze surrounding the anomaly, caused by “*radiance smearing from highly radiant pixels into adjacent pixels (due to the high emitted radiance and the point-spread function of the detectors³), and by scattering of energy within the atmosphere above the active flow surface*” (Wright *et al.*, 2001). This zone of radiance should not be used to map or measure the thermal anomaly character, for the radiance is in pixels where it does not belong and is thus spurious.

³ See Chapter 3 for definition of the point spread function.

AVHRR-class detector response over intense thermal anomalies

The low saturation levels, sensitivity of MIR bands to high temperature sub-pixel sources, and the size and intensity of an active lava source mean that AVHRR-class data acquired in the MIR suffer severely from saturation problems. AVHRR's MIR band (band 3) is nearly always saturated over an active lava flow. Again, this is not helped by the fact that open channels and lava fountains may also be active within the pixel, as well as broad zones of dispersed lava flow. However, in a larger pixel, inclusion of areas of ground at ambient temperatures and lower sensitivity of the TIR to high temperature, sub-pixel sources, often mean that TIR data acquired over active lavas are unsaturated, in spite of the low saturation temperature of AVHRR-class sensors operating in this waveband. However, over the largest and most active lava flows, even the TIR will saturate, as seen in the example given to illustrate image sharpening in Electronic Supplement 10. This example is a DN map for an AVHRR image obtained around five hours after the onset of Krafla's 1984 eruption in Iceland when pixels contained an 8.5 km length of active lava fountain feeding high temperature sheet flow in all directions. The core of the anomaly has DN's less than or equal to the non-zero saturation level of 8 defined for the AVHRR flown on NOAA-7 (see Figure S1.11 for definition of non-zero saturation).

The corollary of widespread saturation in the MIR and TIR for the Krafla case was that the hot spot was so intense that a thermal anomaly was detectable in AVHRR's NIR band (band 2, 0.725 – 1.1 μm), in which it was apparent from a three pixel wide (E-W) by nine pixel long (N-S) thermal anomaly (see Figure S1.10). This was aided by the nighttime conditions, which meant that there was no reflection which usually swamps the emitted signal in this waveband. However, such detections in AVHRR's NIR band are rare; there was only one other documented incidence of emission in AVHRR's band 2 over an active lava between 1980 and 1990, this being over a lava channel active on Kilauea on 22 February 1992, as reported by Flynn *et al.* (1994). Again, the data were nighttime, being acquired at 02:33 Hawaiian Standard Time (HST). The rarity of detection in AVHRR's NIR band is borne out by an analysis of AVHRR band 2 data collected during Etna's 1991–1993 eruption (Harris, unpublished data). The eruption began on 14 December 1991 and continued for 473 days until 30 March 1993. During that time images from 648 satellite passes were collected, of which 308 were cloud-free and showed good thermal anomalies in bands 3 and 4 (Harris *et al.*, 1997b). Emission in band 2 was, however, only found at one pixel in one image, that collected on 6 January 1992 at 03:09Z (i.e., nighttime).

Detection in ATSR's SWIR band, which operates at slightly longer wavelengths (~1.6 μm) is not so uncommon. Wooster and Rothery (1997), for example, display (in their Figure 9) four ATSR 1.6 μm nighttime images acquired during Fernandina's 1995 eruption on which between 1 and 13 pixels are plainly anomalous. The eruption began on 25 January 1995, and lasted for around 10 weeks. In total, 17 nighttime ATSR scenes were collected, of which eight were cloud-free and displayed anomalies in the SWIR (Wooster

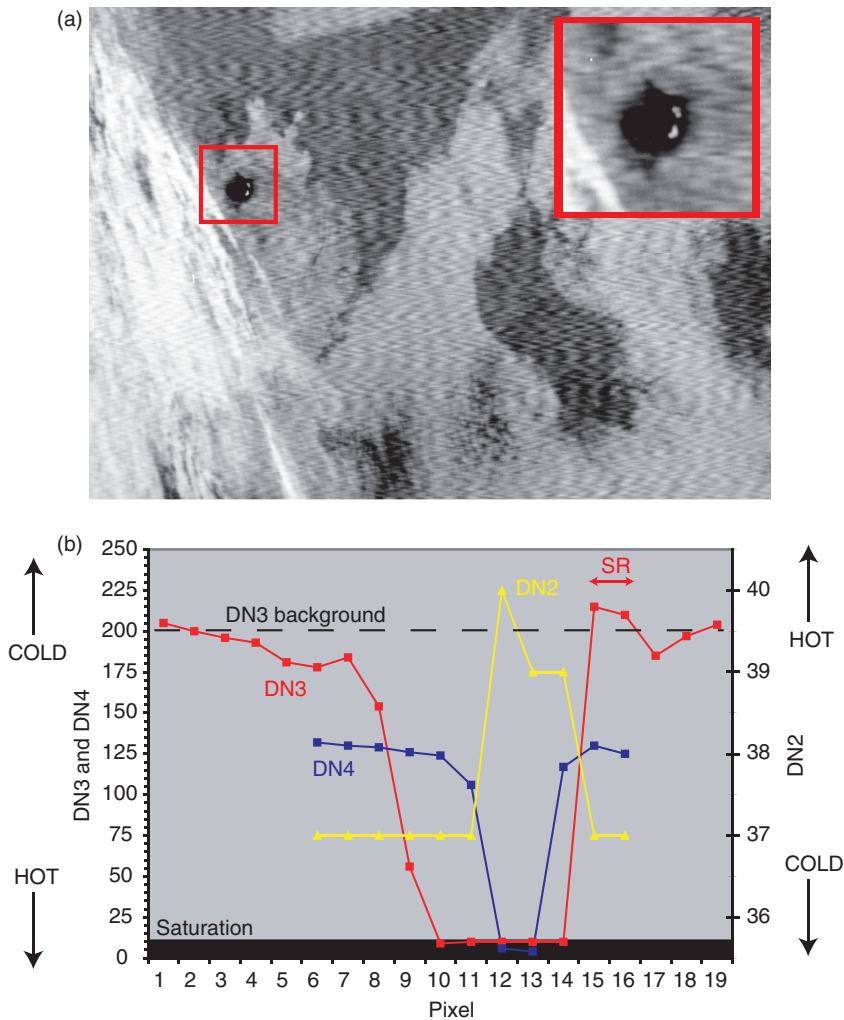


Figure S1.10 NOAA-7 AVHRR MIR (channel 3, 3.55 – 3.93 μm) image of NE Iceland acquired at 04:47Z on 5 September 1984, five hours after Krafla’s September 1984 eruption began. The DN pixel grid for the TIR band of this image (channel 4, 10.3 – 11.3 μm), and information regarding the dimensions of the flow field, are given in Electronic Supplement 10. (a) In the image we see cold cloud advancing from the west (lighter tones relate to lower temperatures), with the image being affected by “herringbone” noise [see Dudhia (1989), Warren (1980) or Simpson and Yhann (1994) for a description of AVHRR noise problems]. Ahead of the cloud bank is the (black) hot spot due to the eruption, as enlarged top right. We see that bleeding causes the anomaly to be badly smeared, and sensor recovery is apparent as a N-S line of white pixels just within the edge of the anomaly on its down-scan (E) edge. These effects are apparent in DN profiles taken across the hot spot, as given in (b). Due to the lower sensitivities of the NIR band (channel 2) and the TIR band (channel 4) bleeding is minimal and the anomaly is much more tightly constrained, being 3–4 pixels wide. Heavy bleeding in the MIR causes an anomaly that is 17 pixels wide, the zone of saturation also being wider than in the NIR and TIR bands by three pixels. We see the sensor recovery effect as a two pixel peak in the down-scan direction of the channel 3 profile (marked SR): note that lower DN’s relate to higher spectral radiances / brightness temperatures in channels 3 and 4, but in channel 2 it is the reverse.

and Rothery, 1997): a much better return than the one AVHRR NIR detection recorded during Etna's 1991–1993 eruption.

Also apparent in Figure S1.10 are the problems caused by radiance bleeding and sensor recovery in AVHRR-class data. The bleeding problem is particularly severe in the MIR, as can be seen from the DN transect of Figure S1.10 where bleeding causes radiance to be spread at least nine pixels in all directions away from the pixels that actually contain the active lava source. This caused the Krafla anomaly to show up as a huge hot spot spread over a large part of NE Iceland (Figure S1.10a). As with the TM data, this radiance halo should not be used to map or measure the thermal anomaly character, for the radiance is in pixels where it does not belong. The sensor recovery problem is apparent in AVHRR data as a group of pixels (usually just one or two pixels wide) with anomalously high DN at the down-scan edge of the anomaly. In Figure S1.10a the sensor recovery pixels are apparent as a group of white pixels within the otherwise dark thermal anomaly caused by the Krafla eruption. As with TM, this is a result of sensor overload over the intense anomaly, causing the sensor response to corrupt immediately down-scan of the anomaly so that a spurious value is recorded. For AVHRR, this results in a small zone of anomalously low radiances, or low brightness temperatures, immediately adjacent to the high radiance anomaly. These corrupt values are unusable in a quantitative sense but may be of value in detection: the incidence of an anomalously low temperature trough immediately adjacent to an anomalously high temperature peak in brightness temperature profiles taken across lava flow related hot spots confirms the presence of a high intensity anomaly associated with the onset of a major effusive eruption.

A third problem found in AVHRR data is that of non-zero saturation. This effect is apparent from non-zero DN cores to a thermal anomaly, when saturation at a DN of zero is expected (e.g., Figure S1.11a). In histograms of DN acquired over thermal anomalies associated with active lavas, non-zero saturation is witnessed as a non-zero mode when a saturated mode of zero is expected, as shown in Figure S1.11b. It affected both the MIR (channel 3) and TIR (channel 4 and 5) in AVHRR, and is apparent as a core of DN = 38 in the channel 3 DN maps for Krafla given in Figure S1.11a. For the AVHRR, it resulted from the sensor not really having been designed for high temperature applications, with the DN registered once the maximum end of the dynamic range was reached not being required to have any specific value (Harris *et al.*, 1995b). The AVHRR sensor was set to register decreasing DN with increasing radiance over a DN range of 0 (highest recordable radiance) to 1024 (lowest recordable radiance). However, Setzer and Verstraete (1994) suggested that, upon reaching the minimum recordable DN, the non-zero saturation effect caused the DN-response to double back on itself so that increasing DN was recorded with increasing radiance beyond a DN of zero. This continued up to 47 DN until the sensor finally capped the value and the recorded DN maxed out. This value varied from sensor to sensor and defined the true (non-zero) saturation level of the sensor. As shown in Figure S1.11, between DN = 0 and the non-zero saturation DN there was thus be a double calibration, one of which was negative (increasing radiance resulting in decreasing DN) and one of

which was positive (increasing radiance resulting in increasing DN). However, because we do not know if we are on the negative or positive calibration function, we cannot use these data. The histogram approach of Figure S1.11b can be used to detect such spurious DN (radiance or brightness temperature) modes indicative of non-zero saturation. If such an effect is detected, all values less than or equal to the non-zero saturation value should be marked as saturated. However, AVHRR/3 was designed so that all over-range signals were mapped to zero (Harris *et al.*, 1995b), so that the problem should just affect NOAA satellite's carrying versions 1 and 2 of the sensor, as listed in Table 1.1 of Chapter 1.

GOES-class detector response over intense thermal anomalies

In spite of the larger pixel size of GOES-class sensors (4 km), lava flow-related thermal anomalies remain relatively easy to detect in the MIR. Figure S1.12 shows an example from Kilauea (Hawaii). In this image a hot spot is apparent in the MIR band (band 2) due to the presence of relatively small areas of active pahoehoe in the pixel, the size, intensity and distribution of the active flows likely being similar to that revealed by the TM image of Figure 6.2 of Chapter 6. The sensitivity of the GOES MIR band to even quite small sub-pixel hot spots thus allows active lavas to be detected even in 4 km pixels. Indeed, the first reports of thermal anomalies in satellite-sensor data were from 64 km² HRIR pixels (see Figure 1.1 of Chapter 1), so this should come as no surprise. Three problems, however, remain.

First we have problems of saturation. The larger pixel size of GOES-class sensors mean that a greater proportion of ground at ambient temperature will be present in the pixel, thereby decreasing the pixel-integrated temperature when compared to TM-class cases where the active lava source often fills the smaller pixel. As a result, some cases which saturate TM-class pixels, will not saturate the GOES-class pixels. However, even quite small active lava flows can force saturation in GOES-class MIR bands. This is apparent from Figure 5.14 of Chapter 5 which is a plot of the maximum MIR radiance recorded by GOES during Kilauea's January 1997 eruption at Napau crater. Saturation is apparent from capping out of the band 2 radiance time series during all but one of the eruptive phases that made up this event. These pixels contained fountain-fed lava flows of quite limited extent, the fissures extending ~2.3 km and feeding lava flows of no more than 800 m in length to cover a total area of 0.239 km². Thus, the lava flows could potentially occupy 1.5 % of a 16 km² GOES pixel, if centered in that pixel, or 0.75 % of a pixel if evenly distributed between two pixels. If effusive events of such limited spatial extent can saturate GOES MIR bands, then we may expect most effusive events to do the same in GOES-class data. Indeed, GOES band 2 radiance plots given by Mougini-Mark *et al.* (2000) reveal, from their flat tops (see Figure 5.15 of Chapter 5), saturation of the MIR throughout the entire 36 day-long effusive eruption of Cerro Azul (Galapagos) in 1998.

Given this saturation problem, the second detection problem encountered in GOES-class data is somewhat contrary: non-detection in the TIR. Simply, the size of the pixel and poor sensitivity of the TIR to sub-pixel hot spots mean that this band does not register an anomaly

(a) Channel 3

799	739	589	360	294	512	679	728
796	695	461	13	36	34	482	651
742	585	197	37	38	38	88	812
697	404	34	37	38	38	38	937
615	225	37	38	38	38	38	858
535	92	37	38	38	38	38	324
493	10	37	38	38	38	37	818
378	33	37	38	38	38	38	739
218	36	38	38	38	38	16	816
139	36	38	38	38	38	184	883
276	33	37	38	38	38	34	953
393	0	36	38	38	38	35	1019
531	275	36	38	38	38	997	878
615	509	273	37	37	190	738	744
643	621	562	357	277	542	712	771

Channel 5

507	503	510	519	517	514	508	500
508	501	506	514	504	504	506	500
509	502	500	490	369	409	505	505
508	499	495	417	11	125	486	510
506	489	476	325	37	20	470	504
505	485	458	127	39	37	444	505
506	489	465	59	39	4	484	500
505	489	430	34	38	280	500	497
502	484	231	39	38	381	503	496
507	488	267	39	38	400	505	494
512	498	436	34	38	315	504	491
510	503	475	7	38	305	505	492
508	507	490	210	73	434	501	493
510	508	503	451	422	489	501	500
516	512	507	499	497	502	505	503

(b)

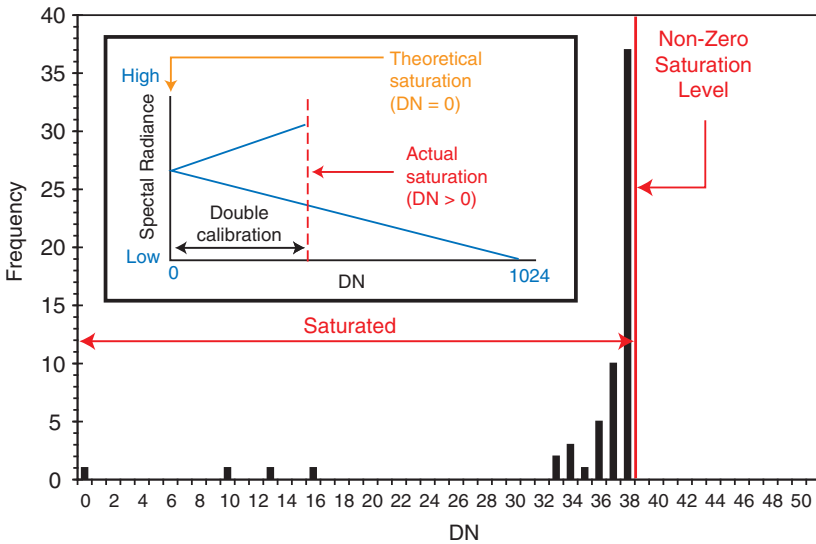


Figure S1.11 (a) DN grids for the “saturated” portion of the NOAA-7 AVHRR channel 3 and 5 image of Krafla given in Figure S1.10a. Pixel dimension is 1.24×1.22 km. Given the radiant intensity of this eruption, all pixels should be saturated, returning a DN of zero. However, only one pixel (highlighted

over smaller active lava flows. The eruption of Napau recorded by the GOES MIR band, for example, did not register as a thermal anomaly in the GOES TIR band (band 4).

The third problem encountered in GOES-class data acquired over active lava is similar to AVHRR's non-zero saturation problem. Termed "rollover" (NOAA Technical Memo), the problem affects channel 2 (the MIR band) of the GOES Imager. It results from a degradation in the sensor over time causing the maximum recordable scene temperature (saturation) and its associated DN to also increase with time. Because the maximum DN that can be registered by GOES is 1023, this causes the DN to roll over once the maximum value has been reached and a very low count value to be transmitted at scene temperatures in excess of the DN=1024 equivalent temperature. NOAA explain the operation as follows: if the radiance value is equivalent to a DN of 1040, then 1040 minus 1024, or 16, is the rolled over value transmitted, which explains white pixels found at the core of intense (black) thermal anomalies found in GOES data.

S1.3.6 Thermal structures and detection of active lava domes and silicic lava flows

Ground-based thermal measurements at active lava domes are rarer than those available for lakes and flows of basaltic lava, mostly due to the difficulty or danger of close approach to the target which may preclude contact measurements. However, available observations support a two component model whereby a chilled, usually blocky or rubblely, crust is broken by hot cracks and/or fumarolic zones. Both Oppenheimer *et al.* (1993b) and Wooster *et al.* (2000), for analyses of TM pixels containing active dome surfaces at Lascar and Unzen, respectively, assumed such a thermal structure. The same two analyses indicated that the crusted component was likely cooler than at basaltic lava lakes and flows, so that SWIR data were largely unsaturated. A 25 March 1990 nighttime TM image of Lascar, given as Figure 11 of Oppenheimer *et al.* (1993b), for example, showed thermal emission in 126 band

Caption for Figure S1.11 (cont.)

in yellow) shows a zero value. All other pixels at the core of the anomaly have DN between 10 and 38 for the channel 3 image, and 4 and 39 for the channel 5 image; these are the pixels highlighted in red (two anomalously cold sensor recovery pixels in the channel 3 image are highlighted in blue). The DN frequency distribution for the channel 3 image is given in (b) and shows a mode at 38. Given that this should be the saturated core of the anomaly, we assume that true saturation occurs at a DN of 38 and the "double calibration" [as inset in (b)] applies, so that over the DN range 0 to 38 two calibration relations apply: one normal and inverse, i.e., decreasing DN relates to increasing spectral radiance; a second spurious and positive, i.e., increasing DN relates to increasing spectral radiance. Because we do not know on which line our DN lies, and the second relation is not defined, we have to assume that all values less than or equal to the non-zero saturation value are saturated. In this case, the non-zero saturation level for channel 3 is 38, and for channel 5 it is 39. The channel 4 DN grid for the same hot spot is given in Electronic Supplement 10 and shows a channel 4 non-zero saturation level of 8. However, DN's in Electronic Supplement 10 are remapped to a 0 to 255 scale, so that, for the 0 to 1024 scale used here, it converts to a non-zero saturation level of 32.

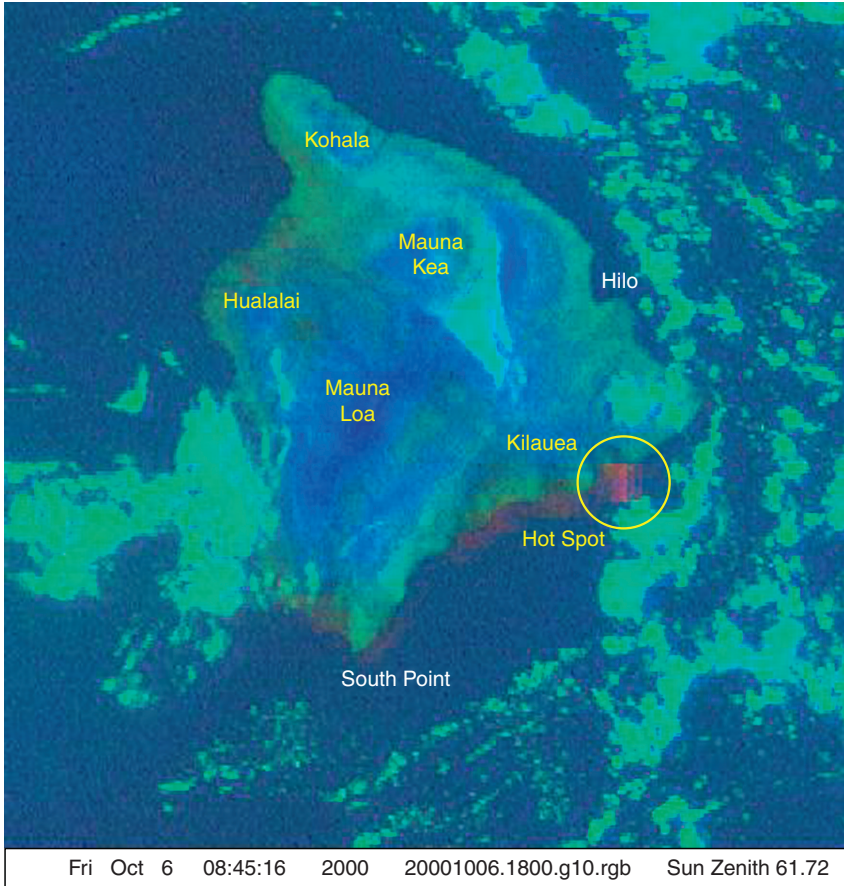


Figure S1.12 GOES band 1 (VIS, 0.55 – 0.75 μm), band 2 (MIR, 3.80 – 4.00 μm), and band 4 (TIR, 10.2 – 11.2 μm) color composite of the Island of Hawaii showing a hot spot due to the emission of tube-fed pahoehoe. In this color composite, the three bands have been assigned blue, green and red, respectively, so that the ocean is dark blue and clouds light blue. While reflection dominates at low elevations, so that the vegetated coastal zones are green, cooler temperatures at higher elevations dominate the signal at the volcano summits (Kohala, Hualalai, Mauna Kea, Mauna Loa and Maun Kea) so that blue marks high ground. The image was acquired at 08:45 local time (18:00Z) on 6 October 2000 so that the ground at higher elevations was still cool, and yet to be severely solar heated. This also allows good contrast between the hot spot and its background. The hot spot in the MIR means that the zone of active lava is apparent as a group of three 4 km red pixels at Kilauea’s coast.

7 pixels. Thirty were also radiant in band 5, only three were saturated in band 7, and none were saturated in band 5.

Field measurements were made of the vent area of Santiaguito’s Caliente “dome” using a radiometer and spectrometer by Sahetapy-Engel *et al.* (2004). The vent zone was actively

extruding lava and was composed of dacitic blocks and rubble, typical of a dome surface. The radiometer measurements indicated typical crust temperatures of between 100 °C and 250 °C, with a typical value of ~125 °C. The spectrometer data showed two types of thermal structure:

- Type 1: A two component thermal structure where a cool crust between 120 °C and 250 °C was broken by hot cracks at ~900 °C, with cracks occupying 0.0026 % of the surface.
- Type 2: An isothermal surface at 350 °C to 500 °C.

Likewise, radiometer measurements made by Oppenheimer *et al.* (1993b) at Lascar lava dome showed hot cracks at ~940 °C, and fumarole vents at 760 °C to 800 °C, the dome being a “roughly circular body of blocky lava ~200 m in diameter” which nighttime observations showed to be “peppered with many glowing sites, distributed in arcuate chains and clusters, mostly close to its margins”.

If we assume the Type 1 thermal structure, we have (for a pixel-filling lava body) pixel-integrated temperatures of,

- In the NIR: 405 – 410 °C
- In the SWIR: 250 – 350 °C
- In the MIR: 250 – 350 °C
- In the TIR: 250 – 350 °C

Thus, dynamic ranges that span 200 to 500 °C should be adequate for detection and thermal measurements of dome surfaces in high spatial resolution (≤ 30 m) pixel data.

If we consider the 200 m diameter of the Lascar dome, the hot spot will fill 3 % of a 1 km AVHRR-class pixel, and 0.2 % of a 4 km GOES-class pixel. Given a dome surface at 120 °C to 350 °C, and the remainder of the pixel at 25 °C, we have pixel-integrated temperatures, in AVHRR-class data of,

- In the NIR: 90 – 280 °C
- In the SWIR: 55 – 190 °C
- In the MIR: 37 – 127 °C
- In the TIR: 30 – 45 °C

Such a feature should thus produce a thermal anomaly (elevated by at least 5 °C above the background) in all wavebands, and, depending on the size and temperature of the surface, the dome target may give unsaturated data. For GOES class data we have,

- In the NIR: 70 – 235 °C
- In the SWIR: 30 – 115 °C
- In the MIR: 26 – 50 °C
- In the TIR: 25 – 26 °C

Thus, for some cases, we are beginning to have no, or a very weak, thermal anomaly in the MIR and TIR. This is consistent with the Santiaguito vent, which was ~150 m across, being extremely difficult to detect in GOES MIR data, and invisible in the TIR.

Silicic lava flows

Silicic lava flows can be even cooler. Observations of silicic lava flows active at Santiaguito between 1999 and 2002 by Harris *et al.* (2002; 2004) showed them to be composed of a thick, cool, blocky-to-rubblery surface, with no nighttime glow. Surface temperature measurements made with a radiometer, as given in Figure 6.24 of Chapter 6, showed crust temperatures declining from 100 – 150 °C near the vent, to a typical value of 25 °C to 60 °C over most of the flow. This makes them undetectable in the SWIR, and extremely difficult to distinguish from a solar heated background in TM-class TIR data. The January 2000 ETM+ image of Santiaguito's active lava dome and flow given in Figure S1.13a shows only a hot spot in the SWIR over the active vent, and no thermal emission along the active lava flow. In the TIR (band 6, Figure S1.13b) we see a weak thermal anomaly down the length of the flow. The band 6 brightness temperature grid, given in Figure S1.13c, shows typical pixel-integrated temperatures in the TIR of 50 to 60 °C, consistent with the field-based measurements made on the same day (the two sets of measurements are compared in Figure 6.24a of Chapter 4). We note, from Figure S1.13c, that pixel-integrated temperatures over solar heated barren, but inactive, lava surfaces on the dome flanks can be as high as those encountered over the active surface.

S1.3.7 Thermal structures and detection of active vents and fumaroles

An active degassing vent is a relatively simple thermal structure, but can be pretty much at any temperature, and can range in size from centimeters to 10s of meters. The exact combination of temperature and size will determine whether the vent can be detected. Vent temperature measurements that I made on Stromboli for incandescent (“puffing”) vents between 1995 and 2001 yielded temperatures between 570 °C and 950 °C, and the vents were typically 2 to 4 m across (Harris and Ripepe, 2007). However, other cold, steaming vents active in the same crater in May 2000 were as low as 40 °C to 200 °C. During June and October 1994 I measured, for an open vent in Etna's La Voragine crater, 300 °C to 340 °C, and 160 °C to 170 °C for a vent in the Bocca Nuova. Both vents were about 10 m in diameter (Harris *et al.*, 1997a). This range of vent temperatures and sizes makes them detectable in TM-class SWIR and TIR data, and sometimes in AVHRR-class MIR data, *if the vent is large and/or hot enough*.

Detection, and levels of thermal emission, will also depend on the activity level of the vent. For example, a vent hosting weak degassing may be relatively cool. However, a vent active with a shallow, vigorously bubbling magma surface, fire fountain or Strombolian eruptions will be relatively hot so that, as in the example of Figure S1.14, the vent may give significant thermal emission in the NIR and SWIR. The vents mentioned above on Etna were detectable as a thermal anomaly in AVHRR MIR data, but not in the TIR data (see Figure S6.1 of Electronic Supplement 6 where the AVHRR brightness temperatures for the summit of Etna on 3 June 1994 are given). Because of the simple thermal structure (hot vent at known temperature against an ambient background), we also use this case to illustrate the basic application of the dual-band methodology in Chapter 4, as well as in Electronic Supplement 6.

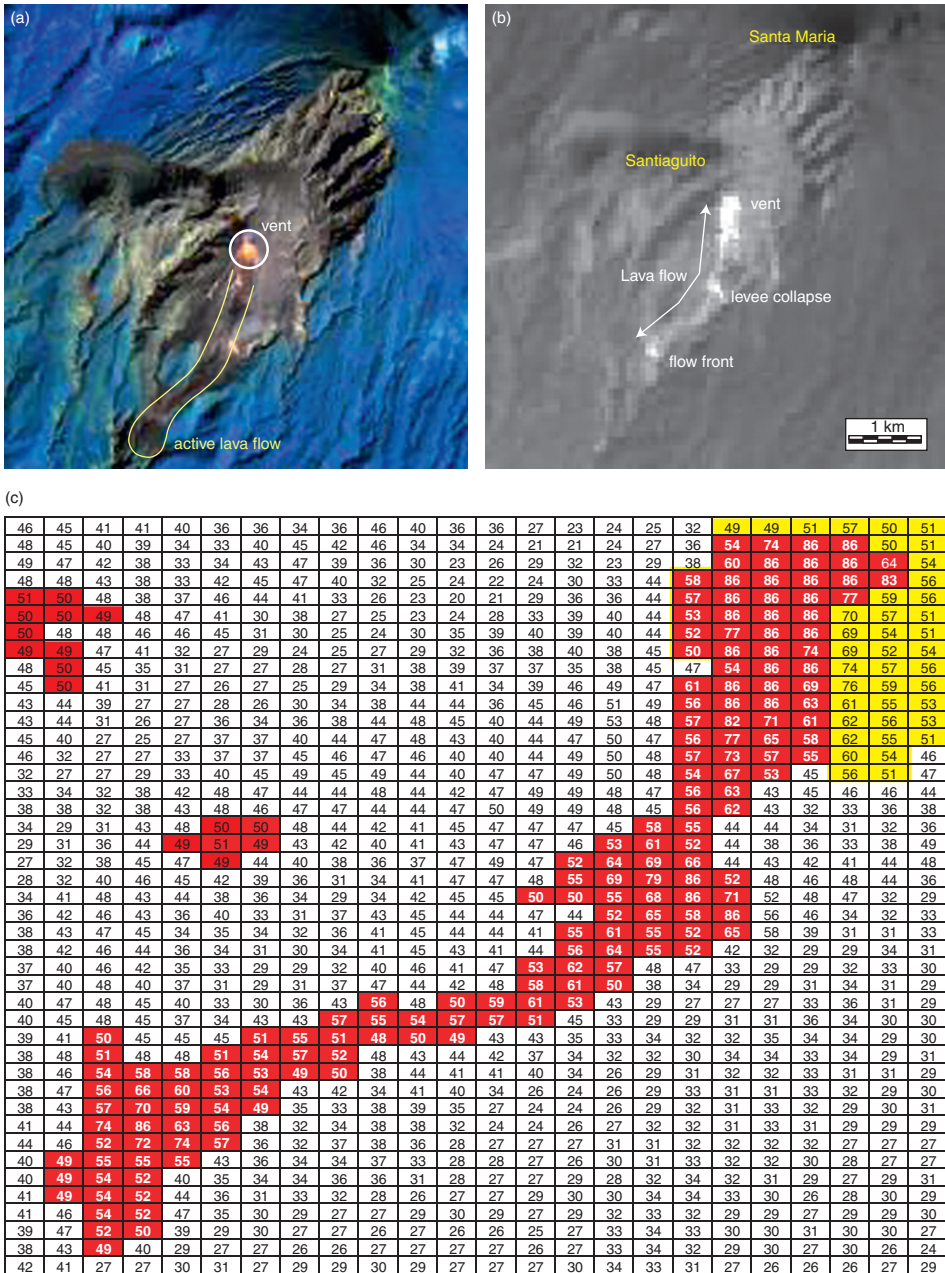


Figure S1.13 Landsat 7 ETM+ image of Santa Maria and the Santiaguito lava dome acquired on 23 January 2000. Image in (a) is a false color composite where bands 7 (SWIR, 2.09– 2.35 μm), 5 (SWIR, 1.55– 1.75 μm), 4 (NIR, 0.75– 0.90 μm) are displayed in red, green, and blue, respectively (see caption of Figure S1.7 for color interpretation key). A dome-like feature over the vent (point of extrusion) causes an unsaturated thermal anomaly in bands 5 and 7 (yellow and red pixels), however the active

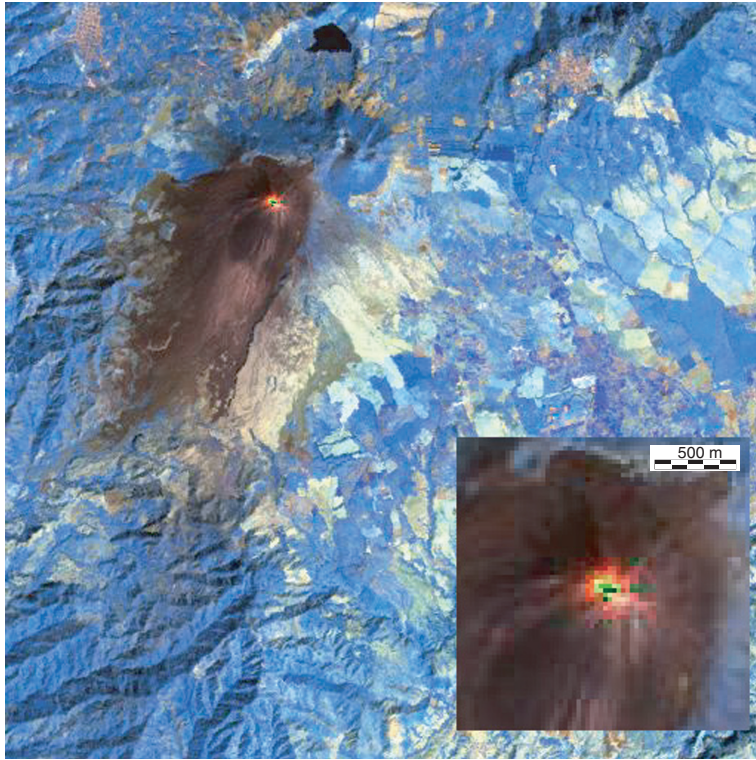


Figure S1.14. Landsat 7 ETM+ image of Pacaya (Guatemala), acquired on 23 January 2000. Image is a false color composite in which bands 7 (SWIR, 2.09– 2.35 μm), 5 (SWIR, 1.55– 1.75 μm), and 4 (NIR, 0.75– 0.90 μm) are displayed in red, green, and blue, respectively (see caption of Figure S1.7 for color interpretation key). A hot spot is apparent in bands 7, 5 and 4 due to intense (near-continuous) Strombolian activity at the vent and a magma surface that is at a very high level.

Caption for Figure S1.13 (cont.)

lava flow is invisible in the SWIR (we have no thermal anomaly). Image in (b) is the 60 m pixel TIR band (band 6) image. We now see three hot spots: one at the vent, one at the flow front, and one due to a levee collapse mid-way up the lava flow. Between these points, the flow itself is a very subtle thermal anomaly. (c) Gives the brightness temperature pixel grid for the active lava flow portion of the band 6 image, allowing us to see the difference between the pixel integrated temperatures for the active lava flow (red pixels – white numbers) and the background (white pixels – black numbers). Two zones in the ambient background (red pixels – black numbers) have temperatures that are the same as those encountered over the active flow. Yellow pixels locate hot dome pixels, where we see there are actually 25 saturated pixels ($T = 86\text{ }^{\circ}\text{C}$) over the vent, but most of the flow is relatively cool and well below saturation. Pixel dimension is 60 m.

Likewise, fumarole vents can range in temperature from 80 °C to magmatic values. The problem is that the vents are usually small (mm to cm in diameter), but, if sufficient vents are active across a fumarole field, a thermal anomaly may be present in the TIR, and possibly in the SWIR. However, even the Vulcano fumarole field, where numerous fumaroles with vent temperatures between 80 °C and 540 °C were active over a ~1600 m² of exhalation between 1994 and 2000 (Harris and Maciejewski, 2000), created only a subtle thermal anomaly in Landsat TM TIR data acquired in the 1990s, no thermal anomaly in the SWIR, and was almost impossible to detect in AVHRR data. Oppenheimer *et al.* (1993a) and Harris and Stevenson (1997) provide further consideration of satellite detection of vents and fumaroles. Harris and Stevenson (1997) were able to produce thermal maps, and complete subpixel temperature estimates and heat flux extractions for open vents at Stromboli using TM data. However, Oppenheimer *et al.* (1993a) concluded that, for fumaroles, although there could be “discernable” response in TM-class SWIR bands, “estimates of subpixel temperatures and heat flux, made from such satellite data, must be considered unreliable”.

S1.3.8 Ocean entry and crater lakes

Crater lakes and ocean water heated by the entry of lava into the ocean can cause the water body to have anomalously high temperatures, detectable as hot (warm) spots in satellite data. However, because the temperatures will be less than 100 °C, detection will only be possible in the MIR and TIR bands. Oppenheimer (1997) showed how crater lakes could be detected in TM-class data by virtue of both their reflective properties in the NIR and SWIR, as well as their thermal properties in the TIR. A DN grid extracted from TM band 6 data for Raupehu’s crater lake is given in Figure S1.15a and shows a 202 pixel (1680 × 2160 m, 2.9 × 10⁶ m²) anomaly with a maximum surface temperature of 20.2 °C, against a background of snow and ice (Oppenheimer, 1997). If we placed this in an AVHRR pixel, it should cause a thermal anomaly covering four pixels. As with the active vent case, whether such an anomaly can be detected in AVHRR-class data will depend on (i) the temperature of the lake surface, (ii) the area of the lake, and (iii) the contrast between the temperature of the lake and that of the ambient background.

Figure S1.15b gives a DN grid extracted from TM band 6 data for a thermal anomaly due to heating of water by entry of lava into the Pacific ocean at Kilauea. We see a 53 (7.63 × 10⁵ m²) pixel anomaly, across which the heated ocean surface is up to 6 °C warmer than the surrounding (ambient) water. However, given that most of the anomaly (~60 % of the pixels) are less than 1 °C warmer than the surrounding ocean, it is unlikely that such an anomaly would be detectable in AVHRR-class data.

S1.4 Saturation: anomaly size, pixel size and wavelength effects

Figure S1.16 provides a simple way to determine how large a sub-pixel hot spot, of given temperature, must be in order to saturate a sensor operating at wavelength λ . To apply this

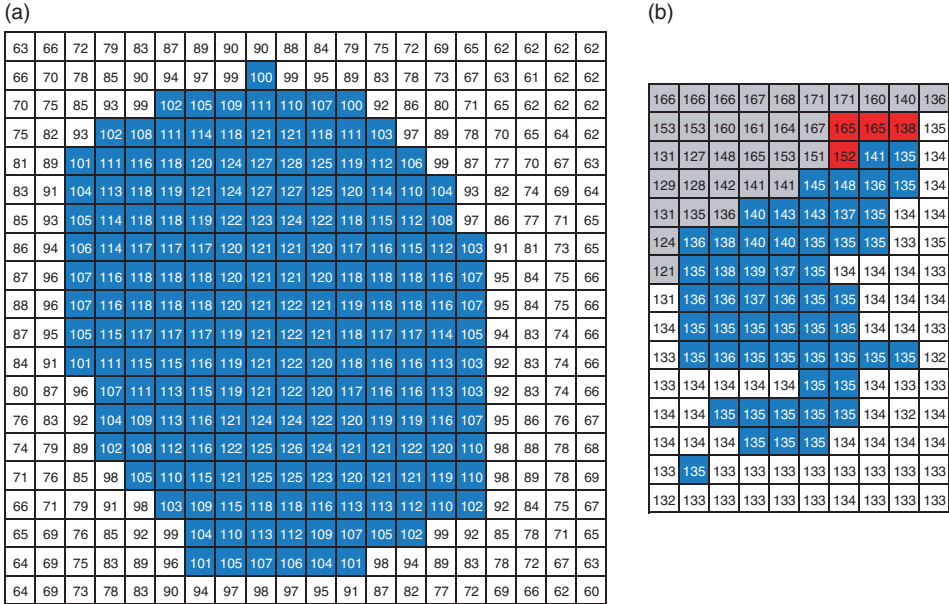


Figure S1.15 (a) TM band 6 DN for a 20 pixel by 20 pixel grid over Crater Lake, Raupehu (New Zealand) from an image acquired on 4 June 1989 [as used by Oppenhiemer (1997)]; thermally anomalous crater lake pixels are blue and pixel dimension is 120 m. (b) TM band 6 DN for a 10 pixel by 15 pixel grid over the Poupou ocean entry active at Kilauea on 23 July 1991, pixel dimension is 120 m. Grey pixels are land (where the location of the coast was fixed using the 30 m SWIR pixels), red pixels are thermally anomalous in the SWIR and locate the point where lava is entering the ocean, blue pixels locate the heated water thermal anomaly, and white pixels are water at ambient temperature. From the orientation of the water anomaly in relation to the point of entry, the water current must be flowing from the NE to the SW.

methodology we take the saturation level of the sensor [$M(\lambda, T_{\text{sat}})$] and place this into Equation (S1.5a), i.e.,

$$M(\lambda, T_{\text{sat}}) = pM(\lambda, T_h) + (1 - p)M(\lambda, T_c) \quad (\text{S1.8a})$$

in which T_{sat} is the sensor saturation temperature. We then rearrange so that,

$$p_{\text{saturation}} = \frac{M(\lambda, T_{\text{sat}}) - M(\lambda, T_c)}{M(\lambda, T_h) - M(\lambda, T_c)} \quad (\text{S1.8b})$$

For a given hot spot and background temperature (T_h and T_c) we can then estimate the level of p required to yield $M(\lambda, T_{\text{sat}})$, i.e., to the size of p required to saturate the pixel ($p_{\text{saturation}}$) at each hot spot temperature.

For a given saturation and background temperature we can do this for the full range of hot spot temperatures, from just above background to magmatic values. This is done in

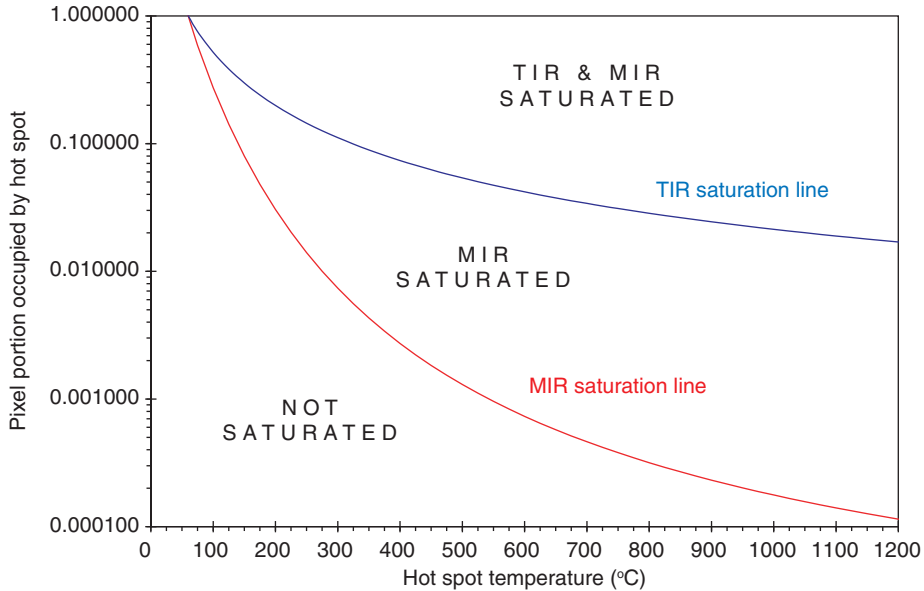


Figure S1.16 Saturation lines defined for the MIR and TIR for a range of hot spot temperatures between 60 °C and 1200 °C, and for a condition whereby the background is at 0 °C and the sensor saturates at 60 °C.

Figure S1.16 and allows us to define saturation lines for each spectral region. These are lines defining, by waveband, the combination of p and T_h at which saturation will occur. Any combination of p and T_h falling below the saturation line will yield unsaturated data; all points above it will saturate the pixel. In Figure S1.16 we have done this for a typical saturation temperature of 60 °C in MIR and TIR data. We see that, due to the decreasing sensitivity to a sub-pixel hot spot between the MIR and the TIR, at any given hot spot temperature, the hot spot can cover a larger pixel portion in the TIR than in the MIR before saturation occurs. For example, a hot spot at 500 °C can occupy 5.4 % of a TIR pixel before forcing a saturation temperature of 60 °C, but will force saturation of a MIR pixel when it covers just 0.13 % of the pixel.

For any given hot spot temperature, the hot spot can also be areally larger in AVHRR-class data than in TM-class data: a 500 °C hot spot will saturate the TIR when it occupies 5.4 % of a pixel. For a 60×60 m ETM+ pixel, this equates to a feature area of 19400 m². However, for the 1000×1000 m AVHRR pixel the area is 5.39×10^6 m². In this case, the greater proportion of cool background in the larger pixel dampens the pixel-integrated intensity of the sub-pixel hot spot emission.

Larger pixels may reduce spatial detail, but they can aid in avoiding saturation, as can use of wavebands at longer wavelengths. As pointed out by Mouginiis-Mark *et al.* (1994), this may mean that a hot spot that saturates an AVHRR-class pixel at nadir, will not cause

saturation at larger scan angles. The increase in an AVHRR-class pixel area from $\sim 1.0 \text{ km}^2$ at nadir, to up to 19 km^2 , when viewed at the scan edge (i.e., at a scan angle of 55°) means that our hot feature can now increase in area to $1.95 \times 10^9 \text{ m}^3$ before it saturates the scan edge pixel. Thus, Mouginiis-Mark *et al.* (1994) argued it may be better to take data at greater viewing angles if we want to avoid saturation over (small) volcanic hot spots such as skylights, vents, domes and lava lakes.

4.5 Detection: viewing geometry effects

For hot spots located in topographic depressions, such as hot vents, lava lakes or domes sited in pit craters or lava flowing beneath a skylight, the hot feature contained within the pit will become increasingly shadowed with increasing view angle. That is, the walls surrounding the hot feature will shield or hide the feature's radiance from the oblique satellite view. For a feature in a pit of depth h , we have the geometry of Figure S1.17 and the hot spot will begin to be shadowed at a scan angle of,

$$\alpha_0 = \tan^{-1} \frac{D}{h} \quad (\text{S1.9a})$$

in which D is the distance between the edge of the hot spot and the base of the pit wall. The feature will then become increasingly shadowed with scan angle until it becomes completely invisible to the satellite view at scan angle,

$$\alpha_0 = \tan^{-1} \frac{(D + w)}{h} \quad (\text{S1.9b})$$

w being the width of the hot feature. As a result, the spectral radiance will decline with scan angle [after the angle defined by Equation (S1.9a)] to become undetectable at the scan angle defined by Equation (S1.9b). At this point, the pit walls completely block the satellite view of the hot spot.

Dehn *et al.* (2002) used this "problem" to their advantage. If we view a conduit containing a shallow magma surface at increasing viewing angles, then the recorded spectral radiance should decrease as a result of increased "shadowing". Thus, if the spectral radiance obtained at any given viewing angle begins to increase, then it should mean that the level of the hot surface in the conduit is ascending, so that more of the feature is becoming visible to the oblique satellite view. Dehn *et al.* (2002) thus used a steady increase in spectral radiance observed in AVHRR channel 3 data prior to the 1999 eruption of Shishaldin to argue that an increase in the magma level occurred in the conduit prior to the eruption.

Such an approach requires that (i) we know the exact geometry of the conduit and/or crater, and (ii) the surface temperature of the hot body within the conduit/crater is stable, as is the conduit/crater geometry. That is, we need to,

- (i) apply a two component mixture model to estimate the pixel portion occupied by the hot body at a temperature of T_h ,

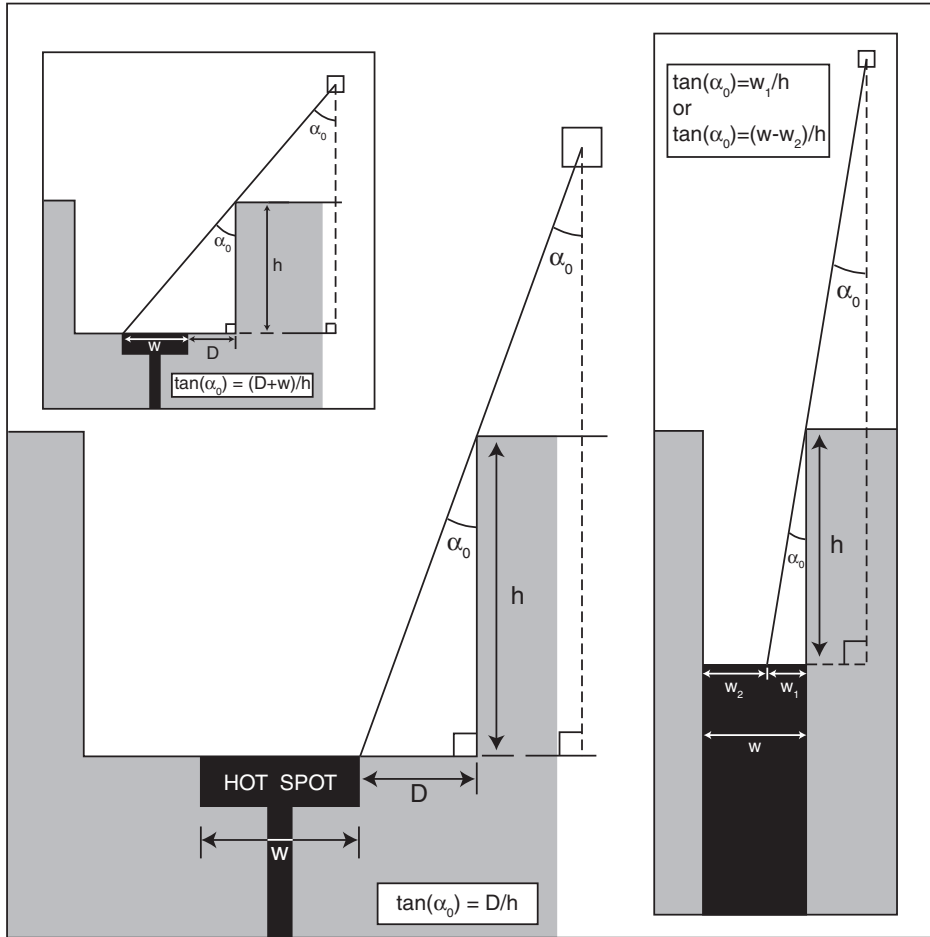


Figure S1.17 Geometry to calculate the point at which a hot spot contained within a pit will begin to be shielded by the walls of that pit when viewed from an off-nadir angle, with (inset top left) the geometry at which the hot spot disappears due to oblique viewing, and (inset right) the geometry used to calculate the depth of a conduit-filling hot body.

- (ii) multiply by pixel area to obtain hot feature area, and
- (iii) assume a shape for the hot feature (or conduit, assuming that the feature is a conduit filler), and reduce the hot feature area to a radius or diameter.

For a simple case, if the diameter of the hot feature is known to be w , and diameter of the obliquely observed hot spot is w_2 , then the depth of the feature in the conduit is (as inset in Figure S1.17),

$$h = \frac{[w - w_2]}{\tan(\alpha_0)} \quad (\text{S1.10})$$

Dehn *et al.* (2002) then used the calculated change in depth with time to estimate a rise rate for the magma surface in the conduit of 14 m per day.

S4.6 A comment on cloud

Detection depends on whether we can see the surface or not. This, in turn, depends on the degree of plume or cloud cover. If there is heavy cloud or plume over the hot spot, then its emission will be blocked from the satellite view and we will not be able to image it. Alternatively, we may be able to detect the thermal anomaly, but contamination by thin or sub-pixel cloud may mean that the extracted radiances are unuseable for quantification purposes (see Chapter 6 for problems caused by cloud contamination in generating time series plots, for example). To assess the problem, we can create cloud calendars, such as that given in Figure S1.18 for AVHRR and TM coverage of Etna’s 1991–1993 eruption.

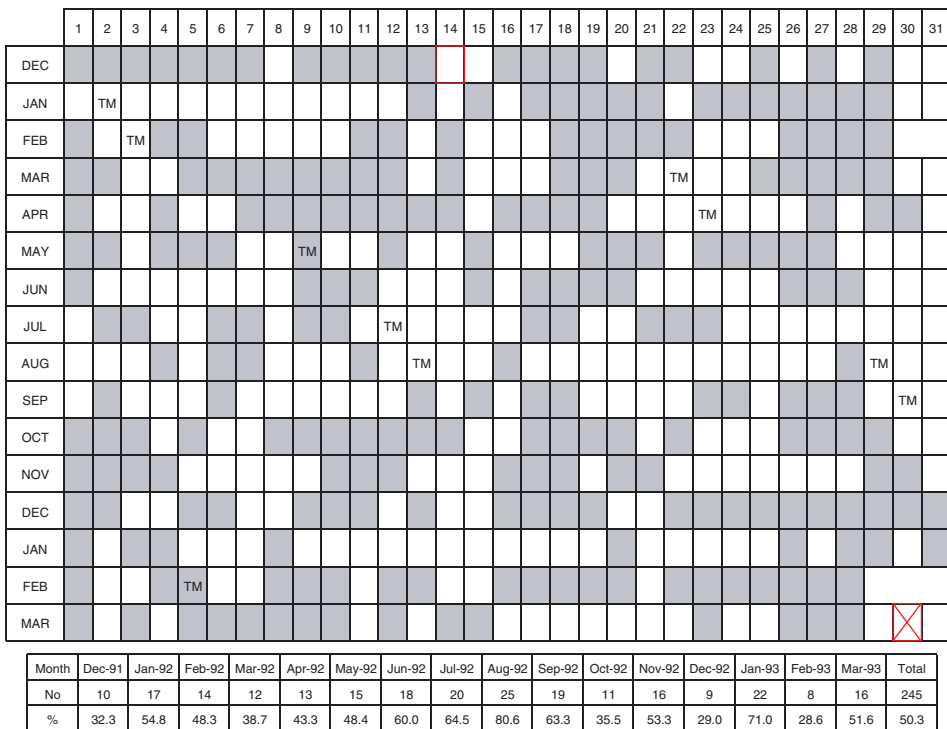


Figure S1.18 Cloud cover calendar for Etna’s 1991–1993 eruption. Gray boxes are days on which no cloud-free AVHRR image was available, and white boxes are days when at least one cloud-free AVHRR image was available. Boxes marked “TM” indicate days on which cloud-free TM images were available, and the first and last days of the eruption are marked using the open red box and the crossed red box, respectively. At the table base are the month by month statistics for the number of cloud-free image days, and the percent of time during which cloud-free imagery was available.

For this case, we see cloud-free coverage is better for certain periods than for others, but that cloud-free imagery was available for 50 % of the eruption days, including the first and last days of the eruption.

In cloudy regions failure to view the target can be a serious problem. For example, in attempting to search for cloud-free images of Jan Mayern volcano (Norway), a volcano that only has 44 clear days per year, Orheim (1993) was only able to find four useable Landsat images between 1972 and 1981, all of which had at least 10 % cloud cover. Note too that, in the SEVIRI-based heat flux time series for an otherwise cloud-free lava fountain at Etna (as given in Figure 5.16 of Chapter 5), the most important (peak) period is lost due to obscuration of the hot spot by a thermally opaque tephra plume that rose above the fountain and its associated lava flows, blocking the satellite view. For such sites and cases, we need to turn to ground-based thermal options, but this is at the cost of the unique cheap, repeat, synoptic, overhead perspective provided by the satellite-based sensor.

References

- Crisp, J. and Baloga, S. (1990). A model for lava flows with two thermal components. *Journal of Geophysical Research*, **95**, 1255–1270.
- Dehn, J., Dean, K. G., Engle, K. and Izbekov, P. (2002) Thermal precursors in satellite images of the 1999 eruption of Shishaldin volcano. *Bulletin of Volcanology*, **64**, 525–545.
- Dudhia, A. (1989). Noise characteristics of the AVHRR infrared channels. *International Journal of Remote Sensing*, **10**(4&5), 637–644.
- Flynn, L. P. and Mouginiis-Mark, P. J. (1992). Cooling rate of an active Hawaiian lava flow from nighttime spectroradiometer measurements. *Geophysical Research Letters*, **19** (17), 1783–1786.
- Flynn, L. P. and Mouginiis-Mark, P. J. (1994). Temperature measurements of an active lava channel from spectral measurements, Kilauea Volcano, Hawaii. *Bulletin of Volcanology*, **56**, 297–301.
- Flynn, L. P. and Mouginiis-Mark, P. J. (1995). A comparison of the thermal characteristics of active lava flows and forest fires. *Geophysical Research Letters*, **22**(19), 2577–2580.
- Flynn, L. P., Mouginiis-Mark, P. J., Gradie, J. C. and Lucey, P. G. (1993). Radiative temperature measurements at Kupaianaha lava lake, Kilauea Volcano, Hawaii. *Journal of Geophysical Research*, **98**(B4), 6461–6476.
- Flynn, L. P., Mouginiis-Mark, P. J. and Kerton, C. A. (1997). Thermal characteristics of a'a flows, Kilauea, Hawaii. *IAVCEI General Assembly*, Puerto Vallaria (Mexico), 19–24 January 1997, abstracts volume, p.60.
- Harris, A. J. L. and Maciejewski, A. J. H. (2000). Thermal survey's of the Vulcano Fossa fumarole field 1994–1999: evidence for fumarole migration and sealing. *Journal of Volcanology and Geothermal Research*, **102**(1–2), 119–147.
- Harris, A. and Ripepe, M. (2007). Temperature and dynamics of degassing at Stromboli, *Journal of Geophysical Research*, **112**, B03205. DOI: 10.1029/2006JB004393.
- Harris, A. J. L. and Stevenson, D. S. (1997). Thermal observations of degassing open conduits and fumaroles at Stromboli and Vulcano using remotely sensed data. *Journal of Volcanology and Geothermal Research*, **76**, 175–198.

- Harris, A. J. L., Vaughan, R. A. and Rothery, D. A. (1995a). Volcano detection and monitoring using AVHRR data: the Krafla eruption, 1984. *International Journal of Remote Sensing*, **16**(6), 1001–1020.
- Harris, A. J. L., Rothery, D. A., Carlton, R. W., Langaas, S. and Mannstein, H. (1995b). Non-zero saturation of AVHRR thermal channels over high temperature targets: evidence from volcano data and a possible explanation. *International Journal of Remote Sensing*, **16**(1), 189–196.
- Harris, A. J. L., Butterworth, A. L., Carlton, R. W., Downey, I., Miller, P., Navarro, P. and Rothery, D. A. (1997a). Low cost volcano surveillance from space: case studies from Etna, Krafla, Cerro Negro, Fogo, Lascar and Erebus. *Bulletin of Volcanology*, **59**, 49–64.
- Harris, A. J. L., Blake, S., Rothery, D. A. and Stevens, N. F. (1997b). A chronology of the 1991 to 1993 Etna eruption using AVHRR data: implications for real time thermal volcano monitoring. *Journal of Geophysical Research*, **102**(B4), 7985–8003.
- Harris, A. J. L., Wright, R. and Flynn, L. P. (1999). Remote monitoring of Mount Erebus Volcano, Antarctica, using Polar Orbiters: Progress and Prospects. *Internal Journal of Remote Sensing*, **20**(15&16), 3051–3071.
- Harris, A. J. L., Flynn, L. P., Matias, O. and Rose, W. I. (2002). The thermal stealth flows of Santiaguito: implications for the cooling and emplacement of dacitic block lava flows. *Geological Society of America Bulletin*, **114**(5), 533–546.
- Harris, A. J. L., Flynn, L. P., Matias, O., Rose, W. I. and Cornejo, J. (2004). The evolution of an active silicic lava flow field: An ETM+ perspective. *Journal of Volcanology and Geothermal Research*, **135**, 147–168.
- Hon, K., Kauahikaua, J., Denlinger, R. and McKay, K. (1994). Emplacement and inflation of pahoehoe sheet flows: observations and measurements of active lava flows on Kilauea volcano, Hawaii. *Geological Society of America Bulletin*, **106**, 351–370.
- Keszthelyi, L. (1995). A preliminary thermal budget for lava tubes on the Earth and planets. *Journal of Geophysical Research*, **100**(B10), 20,411–20,420.
- Mouginis-Mark, P. J., Garbeil, H. and Flament, P. (1994). Effects of viewing geometry on AVHRR observations of volcanic thermal anomalies. *Remote Sensing of Environment*, **48**, 51–60.
- Mouginis-Mark, P. J., Snell, H. and Ellisor, R. (2000). GOES satellite and field observations of the 1998 eruption of Volcan Cerro Azul, Galápagos. *Bulletin of Volcanology*, **62**, 188–198.
- NOAA Technical Memo. GVAR data rollover in channel 2 of GOES-12 imager, NOAA, 8 p.
- Oppenheimer, C. (1997). Remote sensing of the colour and temperature of volcanic lakes. *International Journal of Remote Sensing*, **18**(1), 5–37.
- Oppenheimer, C. M. M. and Rothery, D. A. (1991). Infrared monitoring of volcanoes by satellite. *Journal of the Geological Society of London*, **148**, 563–569.
- Oppenheimer, C., Rothery, D. A. and Francis, P. W. (1993a). Thermal distributions at fumarole fields: implications for infrared remote sensing of active volcanoes. *Journal of Volcanology and Geothermal Research*, **55**, 97–115.
- Oppenheimer, C., Francis, P. W., Rothery, D. A., Carlton, R. W. T. and Glaze, L. S. (1993b). Infrared image analysis of volcanic thermal features: Lascar Volcano, Chile. *Journal of Geophysical Research*, **98**(B3), 4269–4286.
- Orheim, O. (1993). Glaciers of Jan Mayen, Norway. *United States Geological Survey Professional Paper*, **1386-E-6**, pp. E153–E164.
- Sahetapy-Engel, S. T. M., Flynn, L. P., Harris, A. J. L., Bluth, G. J., Rose, W. I. and Matias, O. (2004). Surface temperature and spectral measurements at Santiaguito

- lava dome, Guatemala. *Geophysical Research Letters*, **31**, L19610. DOI: 10.1029/2004GL020683.
- Setzer, A. W. and Verstraete, M. M. (1994). Fire and glint in AVHRR's channel 3: a possible reason for the non-saturation mystery. *International Journal of Remote Sensing*, **15**(3), 711–718.
- Simpson, J. J. and Yhann, S. R. (1994). Reduction of noise in AVHRR channel 3 data with minimum distortion. *IEEE Transactions on Geoscience and Remote Sensing*, **32**(2), 315–328.
- Warren, D. (1989). AVHRR channel 3 noise and methods of its removal. *International Journal of Remote Sensing*, **10**(4&5), 645–651.
- Witter, J. B. and Harris, A. J. L. (2007). Field measurements of heat loss from skylights and lava tube systems. *Journal of Geophysical Research*, **112**, B01203. DOI: 10.1029/2005JB003800.
- Wooster, M. J. and Rothery, D. A. (1997). Time-series analysis of effusive volcanic activity using the ERS Along Track Scanning Radiometer: The 1995 eruption of Fernandina Volcano, Galápagos Islands. *Remote Sensing of Environment*, **62**, 109–117.
- Wooster, M. J., Rothery, D. A. and Kaneko, T. (1998). Geometric considerations for the remote monitoring of volcanoes: studies of lava domes using ATSR and the implications for MODIS. *International Journal of Remote Sensing*, **19**(13), 2585–2591.
- Wooster, M. J., Kaneko, T., Nakada, S. and Shimizu, H. (2000). Discrimination of lava dome activity styles using satellite-derived thermal structures. *Journal of Volcanology and Geothermal Research*, **102**, 97–118.
- Wright, R., Flynn, L. P. and Harris, A. J. L. (2001). The evolution of lava flow-fields at Mount Etna, 27–28 October 1999, observed by Landsat 7 ETM+. *Bulletin of Volcanology*, **63**(1), 1–7.